Summer 2019

The Development of an Integrated Simulation Model on Understandings on the Interaction between Electromagnetic Waves and Nanoparticles

Xiaojin Wang

THE DEVELOPMENT OF AN INTEGRATED SIMULATION MODEL ON UNDERSTANDINGS ON THE INTERACTION BETWEEN ELECTROMAGNETIC WAVES AND NANOPARTICLES

A Thesis
Presented to
The Faculty of the Department of Chemistry
Western Kentucky University
Bowling Green, Kentucky

In Partial Fulfillment
Of the Requirements for the Degree
Master of Science

By
Xiaojin Wang

August 2019

THE DEVELOPMENT OF AN INTEGRATED SIMULATION MODEL ON UNDERSTANDINGS OF THE INTERACTION BETWEEN ELECTROMAGNETIC WAVES AND NANOPARTICLES

Date Recommended June 25, 2019

Yan Cao

Dr. Yan Cao, Director of Thesis

Bangbo Yan

Dr. Bangbo Yan

Dr. Darwin Dahl

Cheryl D. Davis 7/23/19

Dean, Graduate Studies and Research Date

I dedicate this thesis to my parents Zhanhong Wang and Yanqin Wang, who are a great inspiration to me. Also, I also dedicate this work to my advisor Dr. Yan Cao and my friend Dr. Yongqing Wang, who helped me to choose the research topic and build models.

ACKNOWLEDGMENTS

I am appreciated for the people who offered me valuable help during my study and research in WKU.

First, I would like to give my sincere gratitude to my advisor Dr. Cao, and his encouragement, inspiration and patience helped me finish my research. He could always provide me the necessary materials and advice during my study. He was good at giving forward-looking, out-of-box and comprehensive suggestions which helped to broaden my horizons.

I would also like to thank Dr. Bangbo Yan and Dr. Darwin Dahl for being thesis committee members and their helpful suggestions. I would also like to thank Dr. Bangbo Yan, Dr. Yan Cao and Pauline Norris for their interesting and inspiring lectures on chemistry knowledge. I appreciate Dr. Eric Conte and Haley Smith for his careful guidance in my school life. In addition, many thanks for teachers and classmates who gave a lot of advice in the seminar.

Besides, I would like to thank my friends in Dr. Cao's lab. Thanks for the help of visiting scholar Yongqing Wang and Xuxin Yang who contributed to my research modeling work as partners. And I am grateful for Junjie Xiang who helps me adapt to life and study in the US. Finally, I would like to thank my parents Zhanhong Wang and Yanqin Wang for their big support and love.

PREFACE

This thesis is written for my Master's degree at Western Kentucky University. The research described here was instructed by Dr. Yan Cao in the Department of Chemistry, Western Kentucky University, from January 2018 to June 2019. Except for the references, this work is original. Neither this, nor any substantially similar dissertation has been or is submitted for any other degree, diploma.

This research is devoted to the study of the interaction between nanoparticles and electromagnetic waves using a numerical simulation method. Narrowed-down and specific attention in this thesis was given to the interaction between nanoparticles and UV-Vis-IR light, which is of great significance since comparable scales of nanoparticles and the wavelength of UV-Vis-IR. On the other hand, nanoparticles or nanomaterials are widely used in physics, chemistry, biology, medicine, environment and other disciplines. This research is mainly a theoretical method, different from the experimental method, that ensures in-deep understandings on the interaction between nanomaterial and electromagnetic waves, and also great in assisting the explication of experimental results.

In addition, this research expanded the application of the theoretical method, exploring a new technique to study the optical properties of nanoparticles. In this way, the optical properties of nanoparticles can be predicted quickly and accurately. The thesis work shows great potentials of wide applications in the field of solar energy harvest, optical properties of soot, photothermal cancer therapy and so on.

CONTENTS

LIST OF FIGURES

LIST OF TABLES

Nomenclature

σ	cross section
Q	power loss density
Q_{sca}	scattering efficiency
Q_{abs}	absorption efficiency
Q_{ext}	extinction efficiency
ε	dielectric constant
$p(\mathbf{r})$	power density
$k(\mathbf{r})$	thermal conductivity
$T(\mathbf{r})$	temperature
ρ	mass density
c_p	specific heat capacity
h	heat transfer coefficient
a	radius of nanoparticles
I	intensity of penetrated light
I_0	intensity of the incident light
L	depth of suspension
α	absorption coefficient
φ	volume fraction
λ	wavelength of light
μ	viscosity
D_f	fractal dimension
E_{abs}	absorption enhancement

Superscripts

sca	scattering
abs	absorption
ext	extinction
ns	nanoparticle suspension
m	surrounding medium
np	nanoparticle
nf	nanofluids
w	water

Abbreviations

FEM	finite element method
LSPR	localized surface plasmon resonance
SEM	scanning electron microscopy
TEM	transmission electron microscopy
AFM	atomic force microscopy
NTA	nanoparticle tracking analysis
DLS	dynamic light scattering
SLS	static light scattering
MALS	multi-angle light scattering
UV-Vis	ultraviolet-visible
DDA	discrete dipole approximation
PML	perfectly matched layers
DLA	diffusion limited aggregation algorithm
PSL	polystyrene latex

THE DEVELOPMENT OF AN INTEGRATED SIMULATION MODEL ON UNDERSTANDINGS ON THE INTERACTION BETWEEN ELECTROMAGNETIC WAVES AND NANOPARTICLES

Xiaojin Wang August 2019 Pages 51

Directed by: Yan Cao, Bangbo Yan, and Darwin Dahl

Department of Chemistry Western Kentucky University

To investigate the interaction between nanoparticles and electromagnetic waves, a numerical simulation model based on FEM was built in this thesis. Numerical simulation is an important auxiliary research method besides experiments. The optical properties of nanoparticles consist of scattering, absorption, and extinction, and in the case of nanoparticle suspension, the transmission is also involved. This thesis addressed two typical applications based on the established model, one was regarding the nanofluids for solar energy harvesting, and the other was regarding the optical properties of atmospheric soot. In the case of the nanofluids solar energy harvesting, the established model provided a convenient and rapid screening of potential nanoparticles and nanofluids candidates for solar energy harvesting. A core-shell structure nanoparticle, using Cu as the core material in a diameter of 90 nm coated with 5 nm thickness graphene, exhibited a better photothermal property under the solar radiation. In the second case regarding atmospheric soot, the established model provided an efficient method for understandings on the optical properties and warming effects of realistic soot particles. It was found that the sizes and material characteristics of soot, would greatly affect their scattering and absorption of light. Moreover, two submodels were introduced and integrated, which can better predict behaviors of real atmospheric

soot involving their core-shell structures (moisture or organic condensates) and their fractal agglomerate structures. In conclusion, the established model helps to understand the interaction between nanoparticles and electromagnetic waves, which shows great potentials of wide applications.

1 INTRODUCTION

Nanoparticles, are between 1 and 100 nm in size and have potentials of and actual applications in industries because of their unique properties, such as medicine, optics, and electronics and so on. These special properties are largely due to the large specific surface area and the electron confinement effect, which makes these nanoparticles different from those bulk materials and showing size-dependent properties [1]. Especially for noble metals nanoparticles, they have attracted a great more deal of attention due to their localized surface plasmon resonance effect (LSPR), which caused by the collective electron oscillation in the nanoparticle. This makes gold (Au) nanoparticles show a wide range of application prospects, such as the molecular sensing, nanomedicines, the surface-enhanced Raman scattering, the surface-enhanced fluorescence, and the photothermal therapy. Contrastingly, the study of silver (Ag) nanoparticles have been contributing to the application in photonics, data storages, photocatalysis, and sensing technologies. Furthermore, nanoparticles of many other materials, such as other metals, dielectric, semiconductor and their hybrid structures have been widely applied to medicine, physics, optics and electronics [2].

Nanoparticles have different characteristic parameters that affect their physical and chemical properties. For a single nanoparticle, size, shape, crystallinity and composition can deeply influence the properties of nanoparticles and further their applications [3]. In addition, the concentration and size distribution of nanoparticles dispersion system must be measured for its complete description [4]. Two methods have been developed to characterize nanoparticles, namely microscopy and spectroscopy [5]. The microscopy method, addressing the transmission electron microscopy (TEM), the scanning electron

microscopy (SEM) and the atomic force microscopy (AFM), is the most effective in characterizing the sizes and morphologies of nanoparticles, but costly, time-consuming and problematic in the sample preparation leading far away from its original status [6]. This calls for the second method, a fundamental exploratory spectroscopy method, which likely achieves non-invasive and realizing in situ to be introduced. It is largely dependent on the knowledge expansion in the interaction between nanoparticles and electromagnetic waves [7]. The combination method based on both spectroscopy and microscopy, nanoparticle tracking analysis (NTA) enables the direct visualization of nanoparticles in solutions, to precisely investigate particle sizes, size distributions and concentrations of nanoparticles, but lagged by the use of the high cost of microscopes and the loss of morphological information [8] [9].

Many spectroscopic methods for characterizations of nanoparticles are based on studies on scattering, absorption and extinction properties of nanoparticles, both in the time and frequency domains. Dynamic light scattering (DLS) can report the average hydraulic radius of nanoparticles in their suspensions quickly and accurately, which is most applicable only in mono-dispersive systems [10]. Efforts to obtain the size distribution information of nanoparticles lead the development of the algorithm optimization method and nanoparticle separation method [12] [13] [14]. Static light scattering (SLS) which is also known as multi-angle light scattering (MALS) is a group of spectroscopy techniques to obtain the radius of gyration of nanoparticles by measuring the scattering intensity at many angles [15]. These light scattering techniques usually measure the intensities at a fixed angle or multi-angles, angles of backscattering [16] [17], and even the angle in the transmission orientation. However, the information

on scattering lights by nanoparticles is generally difficult to be explained only by the scattering theory. This calls for the assistance of the extinction theory and the Beer-Lambert law and likely dual-wavelength or multi-wavelength techniques, for determinations of sizes and even morphologies of nanoparticles in their suspension systems [20]. Wavelengths in ultraviolet-visible (UV-Vis) spectra ranges can be most convenient to characterize nanoparticles, owing to the sensitivity of the UV-Vis optical properties of nanoparticles in their sizes, shapes, aggregation and components [21]. The UV-Vis spectra have been more applied in characterizations of noble metal nanoparticles such as gold and silver, but little in semiconductors and other nanoparticles [22] [23]. The difference is caused by the existence of the significant LSPR effect of noble metal nanoparticles in the UV-Vis spectra [24] [25]. There are other spectroscopy techniques for characterization of nanoparticles [26] [27], which only applicable in specific situations. Overall, many different spectroscopic methods, bypassing microscopic methods, have been developed based on understandings on the interaction between nanoparticles and electromagnetic waves, although there are no single spectroscopic methods can singly fulfill tasks of determinations of sizes and their distributions and morphologies of nanoparticles.

Prior to address the ultimate task of the determination of sizes and their distributions and morphologies of various nanoparticles, understandings of interactions between electromagnetic waves and nanoparticles must move ahead. Theoretical calculation and numerical simulation techniques seem to be powerful and convenient techniques to address this goal. The theoretical Mie theory has been widely used to explore the interaction between nanoparticles and electromagnetic waves, but limited in

single and spherical-like particles [28]. Thus, many numerical simulation methods have been developed to address the solutions of the most general Maxwell Equation [29] [30]. Among of them, the discrete dipole approximation (DDA), the finite element method (FEM) and the T-matrix are most common ones to be developed in studying on the optical properties of arbitrary nanoparticles as well as their suspensions [31] [32] [33] [34]. In this research, the FEM method was used to investigate the optical properties of nanoparticles and their suspensions, widely involving scattering, absorption and transmission.

FEM is a numerical simulation method which can quickly and accurately solve Maxwell's equations based on a finite difference Yee lattice [35]. The analytical solution of this problem requires the solution for partial differential equations over the domain. (WIKIPEDIA) To solve the problem, it subdivides a large system into smaller, simpler parts that are called finite elements. The simple equations that model these finite elements are then assembled into a larger system of equations that models the entire model. This method can accurately simulate the scattering and absorption of light by nanoparticles, and it can also be coupled with multiple physical fields. For example, the light absorption and heat transfer of nanoparticles can be coupled to simulate the photothermal properties of these nanoparticles which could be used to study photothermal therapy for cancer, solar energy harvest, and warming effect of soot particles. Moreover, it is applicable to physical fields based on different theoretical models. For example, when studying the optical properties of nanoparticle suspension, it can be converted into a model based on Beer-Lambert law for the convenience of calculation.

Therefore, a numerical simulation method based on FEM was established to study the optical properties of nanoparticles and their suspensions in this thesis. The optical properties consist of scattering and absorption of nanoparticles, as well as extinction and transmission of nanoparticle suspensions. In this research, there are two applications of this simulation method, one is regarding the nanofluids for solar energy harvesting, and the other is regarding the optical properties and the warming effect of soot.

2 METHODS AND THEORETICAL MODELS

2.1. Method

The FEM simulation method based on COMSOL Multiphysics was applied to explore the optical properties of nanoparticles and their suspensions. The schematic of the FEM model on the optical of a single nanoparticle is shown in Fig. 1. The nanoparticle was inserted in the surrounding medium, whose external surfaces were set to be perfectly matched layers (PMLs) absorbing all scattered light. The incident light enters the nanoparticle suspension from above. The free tetrahedral grid was selected for simulations of nanoparticle and medium, and the remaining geometry was meshed using the sweep method. The defined maximum element size of the simulation grid was one-sixth of the wavelength of the incident light, and the maximum element size for nanoparticle is 6 nm.

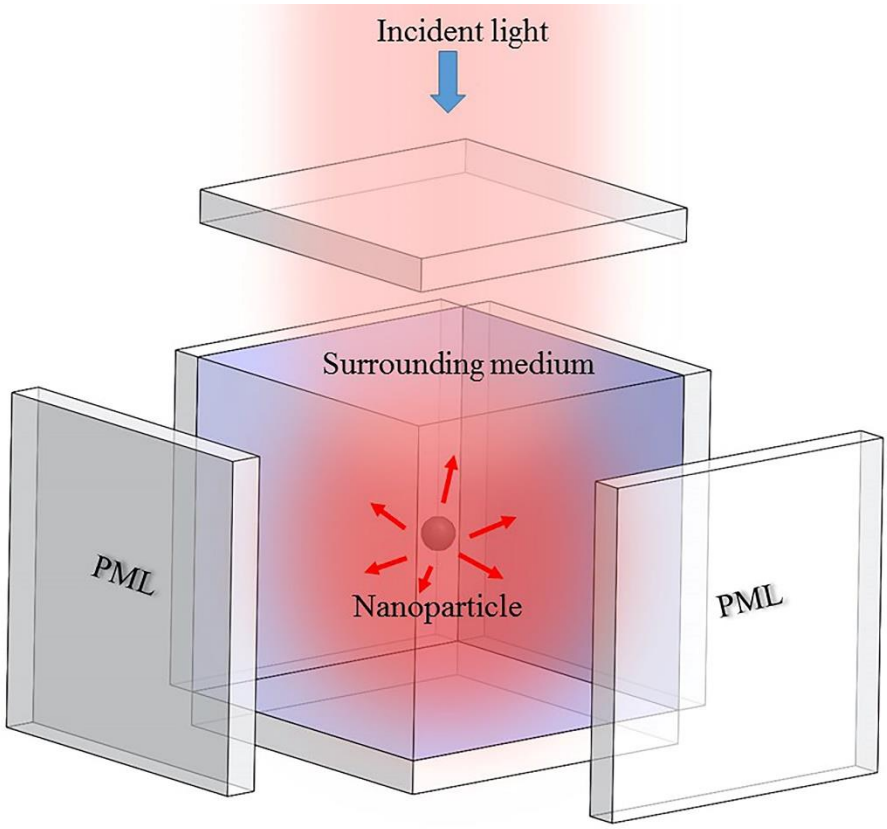

Figure 1. Schematic of the model to study optical properties of nanoparticle and its suspension.

2.2 Optical model of nanoparticles

In order to investigate the optical properties of nanoparticles, Maxwell's equations that govern the interaction of nanoparticles and electromagnetic wave need to be solved. Mie theory is widely used to calculate the absorption, scattering and extinction of nanoparticles undergoing the irradiation of light [36]. In addition, it can be simplified to Rayleigh scattering when the size of nanoparticle is much smaller than the wavelength of incident light. However, they are also suitable for solving spherical-like nanoparticles and the solving process is very complicated. FEM is a numerical simulation method which can quickly and accurately solve Maxwell's equations based on a finite difference Yee lattice [35]. Thus, the electromagnetic field intensity ($\mathbf{E}$ and $\mathbf{H}$) and electromagnetic

flux density ($\mathbf{D}$ and $\mathbf{B}$) can be obtained from the solution, and can be further used to calculate the scattering, absorption and extinction of these nanoparticles.

Solutions of Maxwell equations were further used to calculate the scattering, absorption and extinction cross sections. The scattering cross section σ_{sca} and the absorption cross section σ_{abs} represent the ratio of the entire scattering intensity and absorption intensity of nanoparticles to the incident light intensity, respectively. The scattering, absorption and extinction cross sections can be obtained by

$$\sigma_{\text{sca}} = \frac{1}{I_0}\iint(\mathbf{n}\cdot\mathbf{S}_{sca})dS \tag{1}$$

$$\sigma_{\text{abs}} = \frac{1}{I_0}\iiint QdV \tag{2}$$

$$\sigma_{\text{ext}} = \sigma_{sca} + \sigma_{abs} \tag{3}$$

where $\mathbf{n}$ is the normal vector pointing outwards from the center of the nanoparticle, $\mathbf{S}_{sca}$ is the scattered intensity vector, S is the surface area of the nanoparticle, V is volume of the nanoparticle. Q is the power loss density, which result in heat dissipation in the model. Both $\mathbf{S}_{sca}$ and Q can be derived from the solutions of Maxwell equations. In addition, scattering efficiency Q_{sca}, absorption efficiency Q_{abs} and extinction efficiency Q_{ext} can also be calculated. Q_{sca}, Q_{abs} and Q_{ext} are defined as

$$Q_{sca} = \sigma_{sca}/\sigma \tag{4}$$

$$Q_{abs} = \sigma_{abs}/\sigma \tag{5}$$

$$Q_{ext} = Q_{sca} + Q_{abs} \tag{6}$$

where σ is the projected area of the particle under incident light.

The electromagnetic optical properties of the model depend strongly on their fundamental optical parameters of materials. The experimental approach is only applicable in the acquisition of dielectric constant of bulky or thin film materials, but not for single nanoparticles [37]. Alternatively, the dielectric constant of materials can also be calculated based on the Lorentz-Drude model. This model displays a composite dielectric function ε which includes contributions from both free electron ε^D and the interband term ε^{IB} [38]. Therefore

$$\varepsilon=\varepsilon^D+\varepsilon^{IB}=1-\frac{\omega^2_{pe}}{\omega^2+i\gamma_e\omega}+\sum_j\frac{\omega^2_{pj}}{\omega^2_j-\omega^2-i\gamma_j\omega} \quad (7)$$

where subscript e represents the free-electron, ω_p is the plasma frequency, γ is the damping constant, and the parameter j represent jth oscillator, and ω_j is the resonant frequency of jth oscillator. For nanoparticle equal or smaller than quantum dots (10 nm), the dielectric constant varies with the particle size according to Quantum mechanical model, but can be regarded as size independent upon its size larger than 10 nm [39]. The latter is focused in this study and the dielectric constant from bulk material can be used [40].

Moreover, the absorption of light by nanoparticles causes their temperature to rise based on the electromagnetic loss model, which provides a new characteristic of these nanoparticles. The absorption and heat transfer of particles are easily coupled by FEM model built in this research. The absorption power density $p(\mathbf{r})$ can be obtained by [41]

$$p(\mathbf{r})=\frac{\omega}{2\pi}\,\mathrm{Im}\{\varepsilon(\mathbf{r},\omega)\}|\mathbf{E}(\mathbf{r})|^2 \quad (8)$$

where ω is the frequency of incident light, $\mathbf{r}$ is the position vector. $\mathbf{E}$ is the electric field that can be obtained by solving Maxwell's equations. $\mathrm{Im}\{\varepsilon(\mathbf{r},\omega)\}$ represents the imaginary part of the permittivity of particles. After the absorption power density is obtained, the combined heat transfer equation can be used to solve the temperature of the whole domain. The thermal diffusion equation can be expressed as

$$\rho c_p \frac{\partial T}{\partial t} + \nabla \cdot \left[k(\mathbf{r}) \nabla T(\mathbf{r}) \right] = -p(\mathbf{r}) \tag{9}$$

where $k(\mathbf{r})$ is the thermal conductivity and $T(\mathbf{r})$ is the temperature distribution, both of them are position vector $\mathbf{r}$ dependent. ρ is the mass density, c_p is the specific heat capacity and t is time. Supposed water to be the base medium, owing to the large difference in thermal conductivity between nanoparticles and medium, the Biot number can be calculated as

$$Bi = L_c h / k \tag{10}$$

where h is the heat transfer coefficient, k is the thermal conductivity and L_c is the characteristic length, which is defined as the radius of sphere nanoparticles. When the thermal conductivity of the nanoparticle is much larger than heat transfer coefficient of the nanoparticle/medium interface, then Bi is less than one, leading a nearly uniform temperature inside the nanoparticle and only temperature gradient exists outside the nanoparticle.

$$\Delta T(r) = \begin{cases} \Delta T_{np} \dfrac{a}{r}, r > a \\ \Delta T_{np}, r < a \end{cases} \tag{11}$$

where ΔT_{np} is the temperature increase of nanoparticles, a is the radius of

nanoparticles, r is the distance from the particle center.

2.3. Optical model of nanoparticle suspension

The previous model can effectively and accurately study the optical properties of nanoparticles in a small range. However, it will become more difficult when solving the nanoparticle suspension with large scale. Therefore, a new model based on Beer-Lambert law was introduced. The incident light enters the nanoparticle suspension, and the transmitted light attenuates due to the absorption and scattering of the nanoparticles and the dispersion medium. The Beer-Lambert law, involving the total attenuation process of light propagation in the nanoparticle suspensions, and this process can be modeled as followed,

$$I = I_0 e^{-\alpha_{ns} L} \tag{12}$$

where I is the intensity of penetrated light, I_0 is the intensity of the incident light, L is the depth of suspension in the direction of light penetration, α_{ns} is the absorption coefficient of nanoparticle suspension which can be calculated as

$$\alpha_{ns} = \varphi_m \alpha_m + \varphi_{np} \alpha_{np} \tag{13}$$

where φ_m is the volume fraction of surrounding medium and φ_{np} is the volume fraction of nanoparticles. α_m and α_{np} are absorption coefficient of medium and absorption coefficient of nanoparticle, which can be calculated by [38]

$$\alpha_m = \frac{4\pi\kappa_m}{\lambda} \tag{14}$$

$$\alpha_{np} = \frac{3Q_{abs}}{4a} \tag{15}$$

where κ_m is the imaginary part of the complex refractive index of medium and λ is the wavelength of the incident light. Q_{abs} is the absorption efficiency of nanoparticles. a is the radius of the nanoparticles. Of course, this model varies with different application. When used in nanofluids to absorb solar energy, the surrounding medium is always water, which is non-toxic and readily available. In addition, the density ρ_{nf}, specific heat capacity $(c_p)_{nf}$, viscosity μ_{nf} and thermal conductivity k_{nf} of nanofluids can also be calculated as [42]

$$\rho_{nf} = \varphi_w \rho_w + \varphi_{np} \rho_{np} \tag{16}$$

$$(\rho c_p)_{nf} = \varphi_w (\rho c_p)_w + \varphi_{np} (\rho c_p)_{np} \tag{17}$$

$$\mu_{nf} = (1 + 2.5\varphi_{np} + 6.2\varphi_{np}^{\ 2})\mu_w \tag{18}$$

$$k_{nf} = \frac{k_{np} + 2k_w - 2\varphi_{np}(k_w - k_{np})}{k_{np} + 2k_w + \varphi_{np}(k_w - k_{np})} k_w + \frac{\varphi_{np}(\rho c_p)_{np}}{2} \sqrt{\frac{k_B T}{3\pi a \mu_w}} \tag{19}$$

where ρ_w and ρ_{np} are density of water and nanoparticle, μ_w is the viscosity of water, k_{np} and k_w are thermal conductivities of nanoparticle and water, and k_B is the Boltzmann constant.

2.4. Agglomeration model of nanoparticle

Whether studying the absorption of solar energy by nanofluids or studying the optical properties of soot, it is inevitable to encounter the agglomeration of nanoparticles. For example, the freshly emitted soot particles tend to form aggregates for stabilization during the aging process in the atmosphere. Diffusion limited aggregation algorithm was used to build the nanoparticle aggregation model in this research. The morphology of

particle aggregates also known as fractal equation is defined as follows:

$$N_s = k_f \left(\frac{R_g}{a} \right)^{D_f} \tag{20}$$

where N_s is the number of concerned monomers, a is the mean radius of concerned monomers, D_f is the fractal dimension, R_g is the radius of gyration of aggregates and k_f is the structural coefficient.

3 APPLICATIONS

3.1. Nanofluids for solar energy harvest

Nanofluids, involving nanoparticles of the effective localized surface plasmon resonance (LSPR), exhibit the great enhancement in the light absorption and the heat transfer which activates many technological applications, especially covering solar thermal harvesting. Nanoparticles enhance the thermodynamic and optical properties of water, while water strongly absorbs infrared radiation [44]. This synergistic effect is further enhanced by the applied LSPR-effective nanoparticles. A numerical simulation method integrating classic electromagnetic wave optics, multiparticle group theory, heat transport and the Beer-Lambert law was for the first time established via the built finite element (FEM) model. A variety of spherical and core-shell structured nanoparticles were addressed in aim to control shifts in their LSPR wavelength, targeting the realization of the high extinction efficiency and photothermal conversion at 500 nm wavelength of the highest intensity of solar energy. The validation of the model was established via cross-comparisons among simulating results, the theoretical solution on the simplified Mie scattering and openly-sourced experiment results. The multiparticle

model was also studied to explore the interaction of multiple particles and their contribution to overall photothermal performance under the irradiation. This research provided an efficient method to screen advanced LSRP-effective nanoparticle candidates and optimize the photothermal conversion of nanofluids for solar energy harvest.

3.1.1. Optical properties of the single nanoparticle

Result of the grid independence test for typical gold nanoparticle (50 nm in diameter) is shown in Table 1. Different sizes and the number of grids were adopted to study the influence of the grid parameter on simulation results. The change of the extinction efficiency of 50 nm gold nanoparticle under 500 nm incident light became acceptably minimal when the grid quantity was greater than 42128, indicating the appropriately enough grid distribution. Fig. 2(a) displays the calculated absorption coefficient of water in the spectra of 280 nm-2500 nm, covering the majority of the solar energy. The calculated absorption coefficient of water was significant upon the solar wavelength longer than 1200 nm, implying the only effectiveness of the solar absorption in the far-infrared range by water, and almost transparent in the UV-visible and near-infrared range which is the most energetic spectra of the solar radiation. Fig. 2b, 2c and 2d show the comparison of experiment results [45] [46] [47] and two theoretical calculations (the Mie theory and the FEM) on optical properties (absorbance and the extinction cross section) of Au, Ag, Cu sphere nanoparticles with diameters in 20 nm, 18 nm and 28 nm respectively. The high accuracy of the adopted FEM was exhibited, except for the relatively large deviation for Cu because of its ease in the oxidation. Fig. 2b showed an obvious extinction peak of Au at the wavelength of about 530 nm attributed to the LSPR effect, and at 410 nm of Ag shown in Fig. 2c and at 570 nm of Cu

shown in Fig. 2d. It's apparent that the LSPR-effective nanoparticles exhibited strong extinct in the solar visible light spectra which was not covered by water, and absorbance and the LSPR-effective wavelength shifted upon different nanomaterials.

Table 1. Result of grid independency study for optical model of nanoparticle.

Grid quantity	Extinction efficiency	Difference (%)
18568	2.0168	1.45
42128	2.0465	–
72144	2.0473	0.03
117850	2.0502	0.18
274042	2.0497	0.15

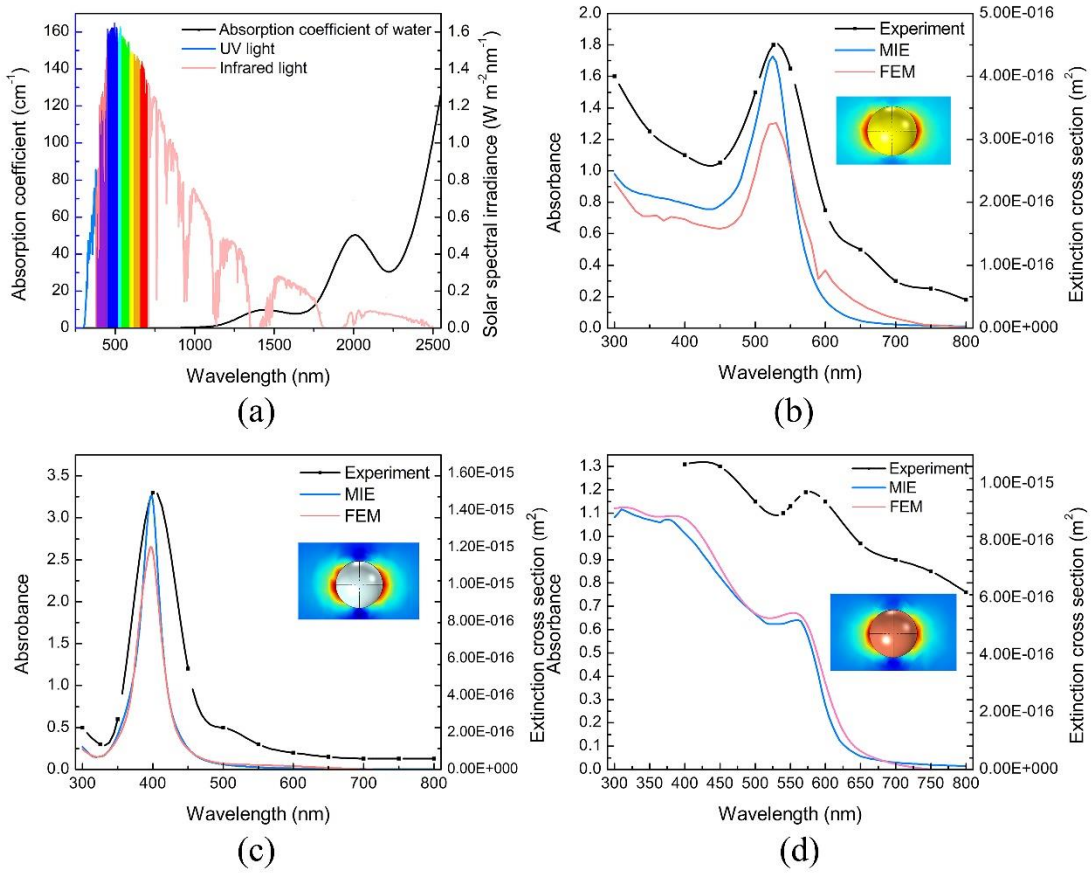

Figure 2. (a) Solar spectrum and water absorption coefficient. (b) – (d) Extinction cross section from FEM and Mie calculations and absorbance from experiments for Au, Ag, Cu nanoparticles.

The LSPR can also be tunable via optimizing the size and the shape of nanoparticles, because of the size-independent character of dielectric constant of nanoparticles. The LSPR shift can solely be attributed to the retardation effect of the size or shape of the particle upon its size larger than 10 nm. Fig. 3a and Fig. 3b show the size-dependent extinction properties of Au nanoparticles from Jiang's experimental results, versus the calculated extinction efficiency of Au nanoparticles based on the FEM method. The LSPR peak shifted clearly from 510 nm to 537 nm when the sizes of Au nanoparticle changing from 4.35 nm to 42.74 nm. Both experimental and simulation results confirmed only a small LSPR shift corresponding to the size change of nanoparticles, exhibiting less effective in the size change for the optimization of the LSPR shift. On the other hand, the electric field analysis, as exhibited in Fig. 3c, revealed the drastic distinction of optical scattering of a single nanoparticle with size increasing, referring to the variation of the oscillator mode from dipole to quadrupole.

Fig. 4a shows the significant LSPR shift of core-shell nanoparticles versus insignificant shift of noble metal nanoparticles. For example, the LSPR peak of Ag nanoparticle shifted from 407 nm to 500 nm, upon an increase of its diameter from 30 nm to 100 nm. In contrast, the 30 nm silica (SiO_2) core coated with only 8 nm Ag in thickness can realize a LSPR effect to 500 nm, also narrowed its extinction spectral. The extinction spectral was broadened when the SiO_2 core increased to 40 nm and Ag shell increased to 28 nm. Cu/Ag 30 nm/35 nm core-shell, Au/Ag 30 nm/35 nm core-shell, graphene/Ag core-shell nanoparticles showed similar extinction efficiency compared with those of SiO_2/Ag core-shell nanoparticles in same core diameter and coating thickness. Optical properties data of graphene in the current simulation were from

Weber's paper [48]. In contrast, the LSPR shift effect became less when core-shell materials switched to noble metal (Ag and Cu) as the core material and SiO_2 or graphene as the shell material as can be seen in Fig. 4b. This study validates a proper design of core-shell nanoparticle was able to control ideal LSPR effect at 500 nm by tuning the core-shell filling ratio and materials.

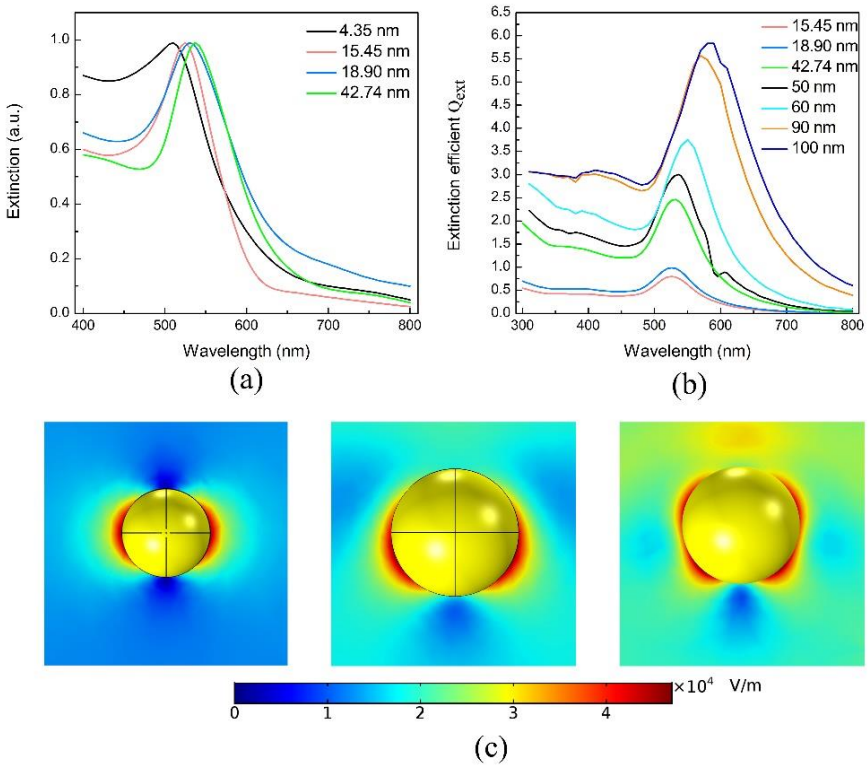

Figure 3. (a) The size-dependent extinction properties of Au nanoparticles from Jiang's experiment results. (b) The size-dependent extinction properties of Au nanoparticles based on FEM method. (c) Scattering field of a single Au nanoparticle with size 50 nm, 10

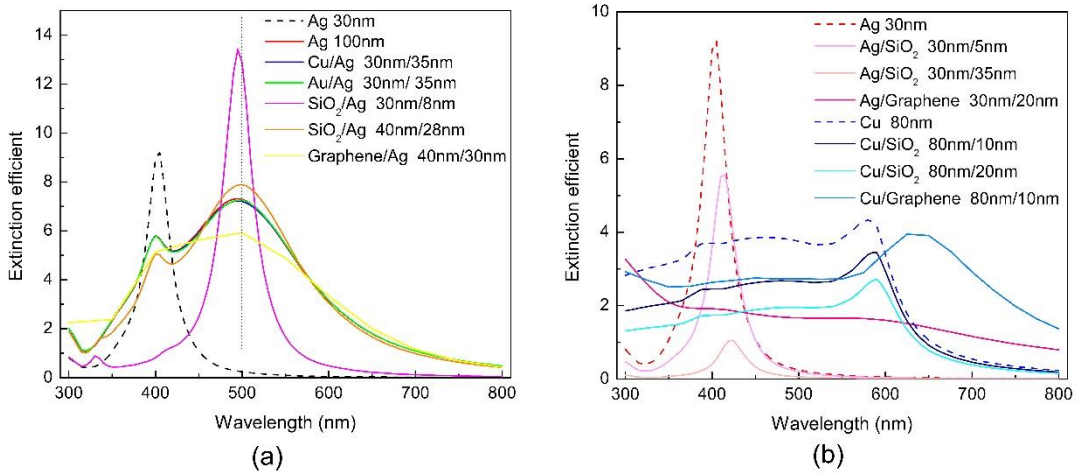

Figure 4. (a) Extinction efficiency of core-shell nanoparticles with noble metal as shell. (b) Extinction efficiency of core-shell nanoparticles with noble metal as core.

3.1.2. Photothermal properties of nanoparticles

Photothermal properties of nanoparticles are regarding the coupling of electromagnetic optics and heat transfer of nanoparticles, involving not only optical characteristics of nanoparticles such as absorption and scattering, but also thermal properties such as thermal conductivity, thermal capacity and convection heat transfer coefficient, etc. Simulation on photothermal properties of a single nanoparticle is initialized with a model shown in Fig. 1. The simulation involved selected noble metal nanoparticles with/without core-shell structures by coupling optical and heat transfer modules. Fig. 5 shows the average equilibrium temperature of the defined physical domain of involved nanoparticles. Among of them, Fig. 5a, Fig. 5b and Fig. 5c exhibit temperature rises of three noble metal nanoparticles (Au, Ag, and Cu), respectively. Results indicated their temperature rises were consistent to their optical extinction as aforementioned in the previous section, and the Au nanoparticle had a higher extinction and photothermal conversion efficient and occurred at 500 nm wavelength, versus that

of the Ag nanoparticle at 400 nm. It was interesting to see a more balanced and efficient photothermal conversion ability of the Cu nanoparticle. Generally, the temperature rises significantly with the increased size of the noble metal nanoparticle. Fig. 5d exhibits the temperature rise of different core-shell nanostructures, indicating the inconsistency of their photothermal properties and optical extinction properties (LSPR at 500 nm wavelength shown in Figure 4a). This study revealed the necessary integration of the thermodynamic properties of the core-shell nanoparticle into the optical extinction model to investigate a joint photothermal effect on the core-shell nanostructure.

Further investigation revealed that Au and Cu noble nanoparticles were most efficient for photothermal conversion in the visible solar spectrum. However, they face challenges in either high cost or easily oxidized respectively when used for the solar energy harvest. Alternatively, the environmentally-sensitive Cu nanoparticles can be encapsulated in graphene or SiO_2 to prevent from the oxidation. Fig. 6a shows the simulated average equilibrium temperature in the physical domain of Cu/Graphene core-shell nanoparticles with the same diameter but different core-shell ratio. Results indicated that Cu nanoparticle in diameter 90 nm and coating with graphene in 5 nm thickness had a better photothermal property, such as a huge increase of its temperature at the wavelength of 600 nm and also satisfactory wavelength coverage reaching as far as 400 nm and 500 nm. Moreover, Fig. 6b further revealed that the photothermal performance of Cu/SiO_2 core-shell nanoparticle was not as good as that of Cu/Graphene core-shell nanoparticle.

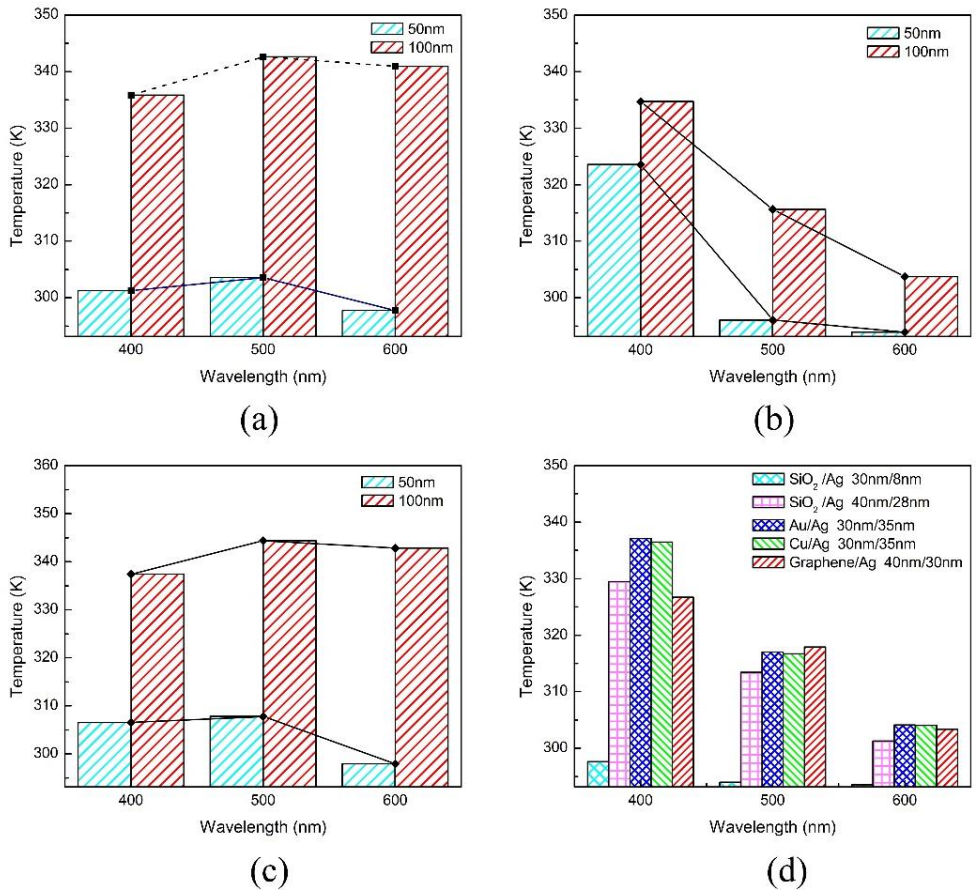

Figure 5. The average temperature of simulated physical domain. (a) Au. (b) Ag. (c) Cu. (d) Core-shell nanostructure.

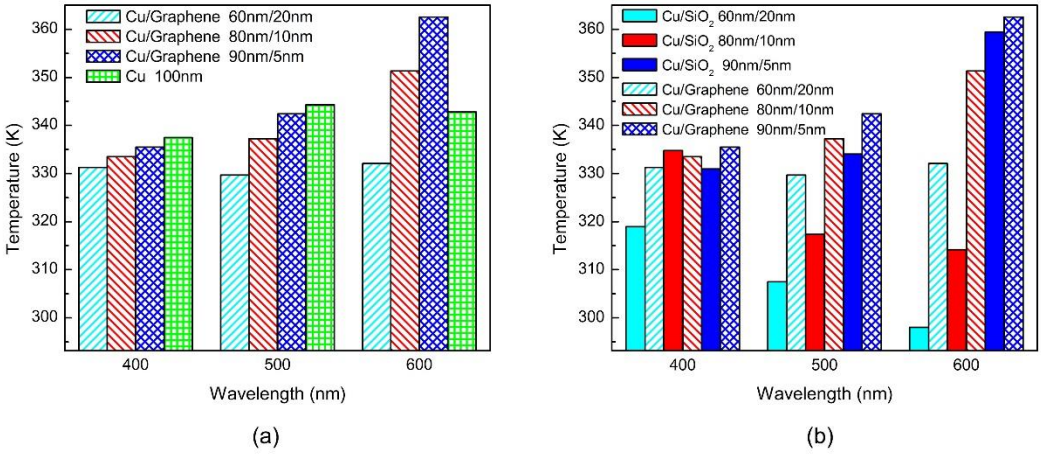

Figure 6. (a) The average temperature of simulated physical domain for Cu and Cu/Graphene

core-shell nanoparticle. (b) The comparison of average temperature of simulated physical domain for Cu/SiO2 and Cu/Graphene core-shell nanoparticles.

As concerned with the multiply-nanoparticle system, aggregation of nanoparticles was inevitably considered. Many different aggregates were formed in these multiply-nanoparticles systems, which significantly impacted on their photothermal properties. For convenience, a two-nanoparticle model was initially established to study the interaction of adjacent nanoparticles. The distance between two nanoparticles, shown as d in Fig. 7a and Fig. 8a, was set to be 0 nm, 60 nm, 100 nm, 160 nm, respectively. Fig. 7b shows the volume average equilibrium temperature in the simulated physical domain increased upon the increase of d. The volume average temperature was 360.51 K when d equals to 0 nm, versus the temperature of 342.44 K for the single nanoparticle (Cu/Graphene 90nm/5nm) case under the similar 500 nm incident light. This implied the heat absorption and heat transfer efficiency of the two-particle system was better than that of a single nanoparticle. However, the temperature gradient in this domain was very small for both cases despite the big difference in their equilibrium temperatures as shown in Fig. 7c. The similar results, as shown in Fig. 8, can also be found true when two particles followed the direction of its connection parallel to the incident light. It was noticeable that this orientation made the first nanoparticle aligning with the incident light, affecting the optical absorption of the second followed one, resulting in the volume average temperature of the whole two-nanoparticle system varied with the distance between two particles, as shown in Fig. 8c. It was also found that the temperature rise of the whole domain was resumed when d became larger than 160 nm.

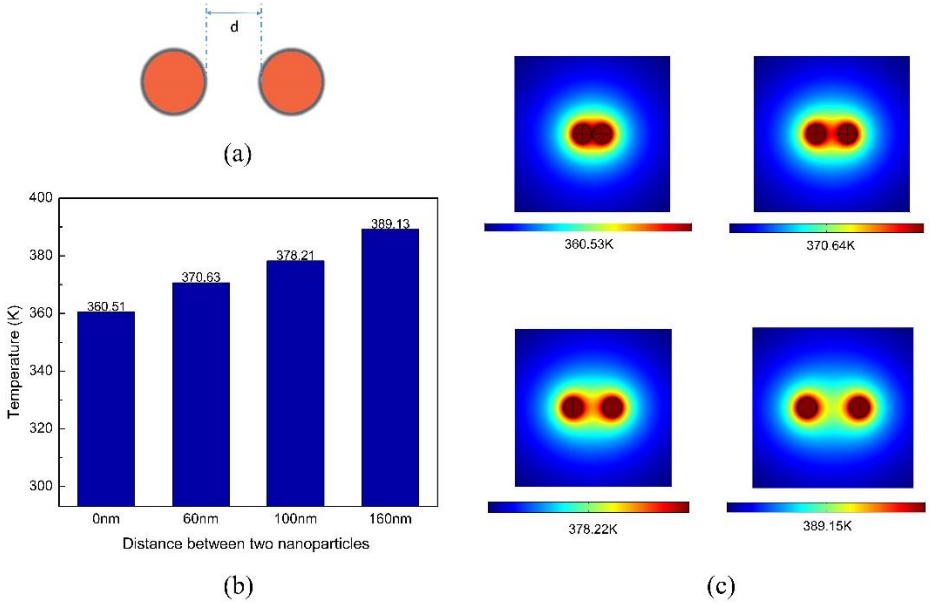

Figure 7. Fig. 7. (a) Schematic of two horizontal nanoparticles. (b) Volume average equilibrium temperature in the simulated physical domain. (c) Temperature field distribution for d = 0 nm, d = 60 nm, d = 100 nm, d =160 nm.

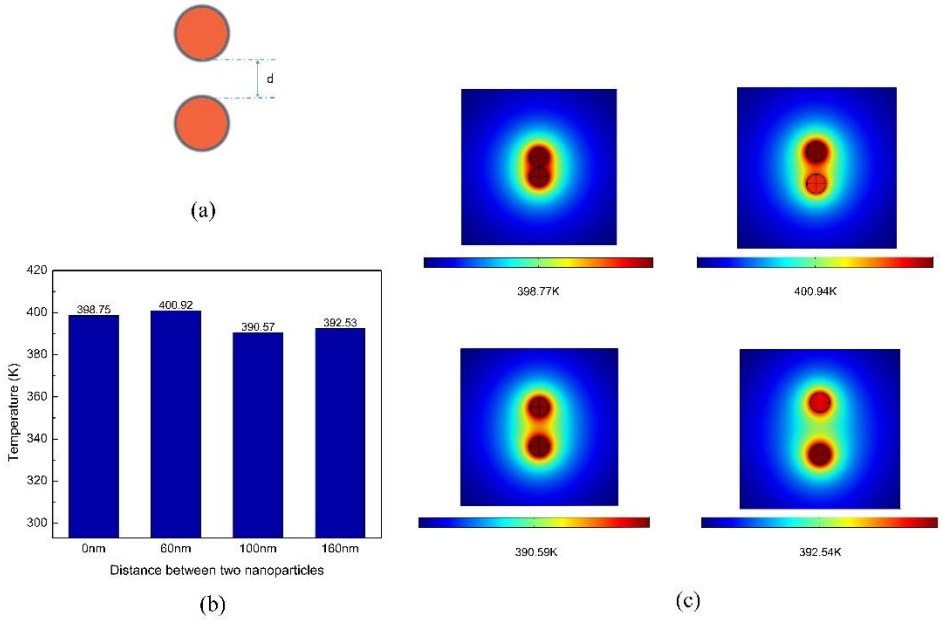

Figure 8. (a) Schematic of two vertical nanoparticles. (b) Volume average equilibrium

temperature in the simulated physical domain. (c) Temperature field distribution for d = 0 nm, d = 60 nm, d = 100 nm, d =160 nm.

This work further dealt with more complex multiply-nanoparticle aggregation system, in which a multiparticle agglomeration model was established based on the DLA [49], which is the based on Brownian motion to establish particle aggregates [50]. Fig. 9a shows an eight-particle aggregation model due to the limited computer resource. The confirmation of this model unit promoted it further being imported to the photothermal model to calculate the photothermal properties of multiply-nanoparticle aggregation system. The simulation conditions were consistent to those of the single nanoparticle model, and phase transition of surrounding medium was ignored to avoid the computational complexity. Fig. 9b shows the energy flux in all directions of the simulated system, in which the energy flux varied with the position and the size of the red arrow is proportional to the magnitude of energy flow. The iso-temperature surface map, representing the temperature distribution, is shown in Fig. 9c. The average equilibrium temperature of the simulated domain reached over 500 K, implying a significant impact of the aggregation of a multiply-nanoparticle system on the light absorption and the heat transfer compared to those of one single nanoparticle system. In addition, the eight-particle uniform distribution model was also computed and its temperature can reach over 700 K as shown in Fig. 9d. Moreover, the volume average equilibrium temperature varied with the polar angle θ and azimuthal angle β of the incident light, as shown in Fig. 10. After reviewing results from the single-nanoparticle, two-nanoparticle and multiply-nanoparticle systems, an overall conclusion can be drawn on the greatness of the impact of the nanoparticle aggregation on the local temperature

rise. Moreover, highly dispersed nanoparticles were preferred for their overall photothermal performance when the volume fraction of nanoparticles was same.

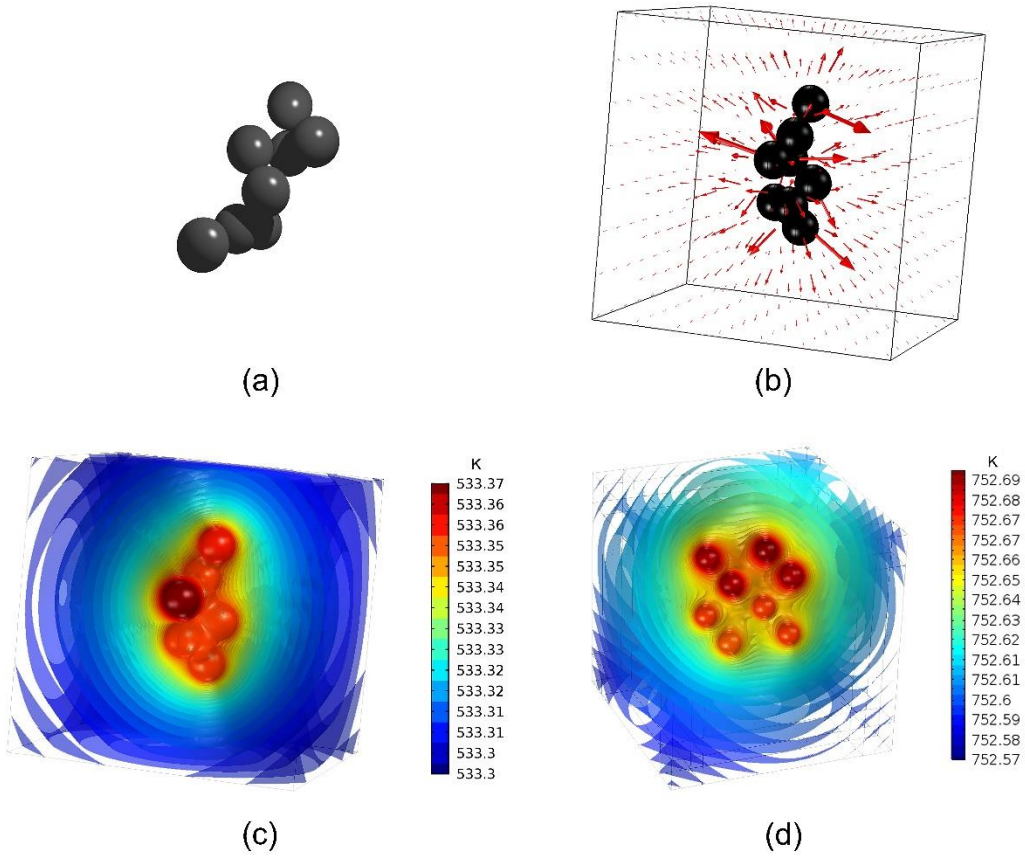

Figure 9. (a) An eight-particle aggregation model from diffusion limited aggregation algorithm (DLA). (b) Energy flux distribution in all direction. (c) Isosurface map of the temperature distribution of eight-particle aggregation. (d) Isosurface map of the temperature distribution of uniform eight-particle model.

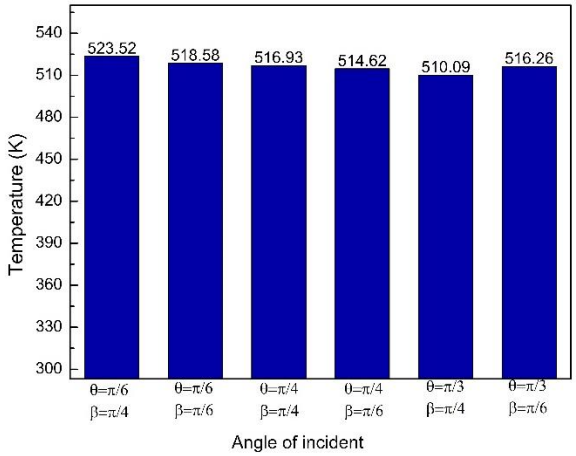

Figure 10. Volume average equilibrium temperature varied with the polar angle θ and azimuthal angle β of incident light.

3.1.3. Photothermal properties of nanofluids

Nanofluids are mixtures of the base fluid with lots of nanoparticles. Their photothermal properties can be experimentally investigated in terms of the Beer-Lambert law. Following-up the previous sections where the copper-graphene core-shell nanoparticle candidates in excellent optical and photothermal properties were introduced for the purpose of the solar energy harvest. Photothermal properties of corresponding nanofluids were further discussed based on the established FEM simulation method. The accuracy of this simulation method was verified through its comparison with experimental results from two open-sources [51] [52]. The first was the temperature rise of a 3 ml thin layer of the Cu nanofluid underneath the center spot of the solar simulator, as shown in Fig. 11. It was found our simulation results on the temperature rise of the sample were agreeable to experimental results, which was nearly 9 K after the 300 seconds irradiation. The second was the Cu nanofluid samples in a

thermally-insulated cylinder test tube underneath of the outdoor natural sunlight. Its temperature distribution and temperature rises of both experiment and simulation were shown in Fig. 12. Fig. 12b revealed an acceptable agreement between the results of experiment and simulation. Their difference may be attributed to uncontrollable environmental conditions and less known on the change trend of solar radiation. The free tetrahedral grids were adopted in both of these models. Grids in numbers of 25667 and 84562 were used in the two models respectively, and the results of grid independency study are shown in Table 2 and Table 3. There was nearly no change in the difference of the volume average temperature after irradiation when the number of grids was further increased. The validation of the simulating method was followed-up to be applied to photothermal properties for our own nanofluids.

Table 2. Result of grid independency study for dish model.

Grid quantity	Temperature (K)	Difference (%)
925	301.59	0.06
4740	301.44	0.01
25667	301.4	–
143127	301.39	0.003

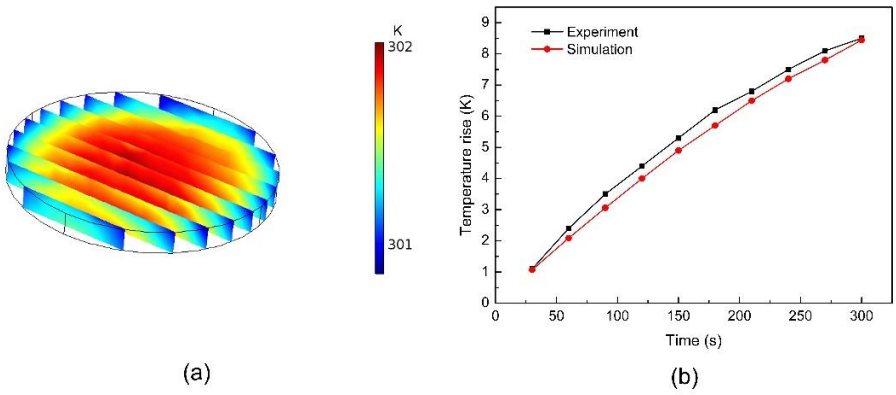

Figure 11. (a) Temperature distribution of the dish model. (b) The temperature rise results from

experiment and simulation for dish model.

Table 3. Result of grid independency study for tube model.

Grid quantity	Temperature (K)	Difference (%)
5350	384.83	6.45
11490	371.45	2.75
43964	362.56	0.29
84562	361.48	–
171359	359.88	0.44
586513	358.8	0.74

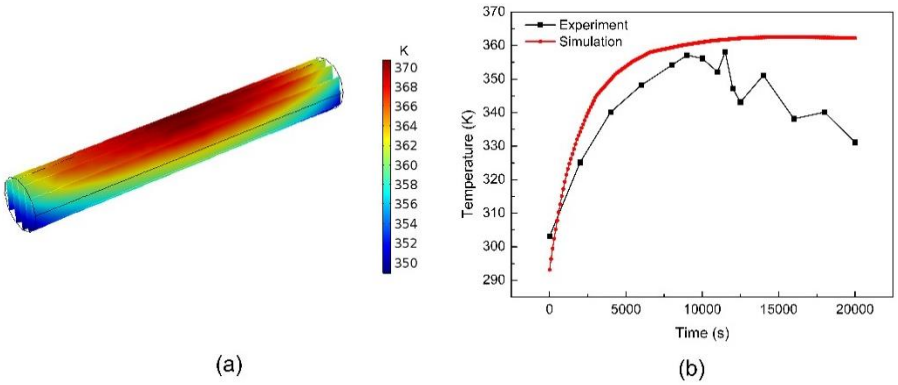

Figure 12. (a) Temperature distribution of the test tube model. (b) The temperature from experiment and simulation for test tube model.

Current interested core-shell nanoparticle fluids had a domain with the length, width, and depth at 500 mm, 100 mm and 100 mm, respectively, corresponding to a three-dimension cuboid in the established simulation model. The visible light entered through its upper surface, with its intensity was set to be 5000 W/m^2. Other surfaces were set to be opaque and insulated. Several kinds of interested nanofluids were selected including CuO, TiO_2/Ag, CuO/Ag, SiO_2/Ag and Cu/Graphene core-shell nanoparticles. Similarly, the free tetrahedral grid was used in this model. The grid independency test result is shown in Table 4, indicating that applied 681788 grids were appropriate in this

model. The photothermal properties of CuO and TiO_2/Ag core-shell nanoparticles fluids were experimentally studied by Yu and Xuan which showed a good photothermal performance [53] [54]. As shown in Fig. 13a, it was found that the temperature of other nanofluids were never greater than 320 K, versus that of the Cu/Graphene core-shell nanoparticle fluid up to 328 K under all same condition after the 1000 seconds irradiation, which revealed a best photothermal performance of the Cu/Graphene nanofluid. Fig. 13b shows the temperature distribution of the simulation domain for nanofluid corresponding Cu/Graphene core-shell nanoparticle and the volume fraction φ =0.01%.

Table 4. Result of grid independency study for cube model.

Grid quantity	Temperature (K)	Difference (%)
82991	361.46	10.23
245939	340.32	3.78
308220	337.7	2.98
393512	334.03	1.86
681788	327.92	–
1342481	326.02	0.58

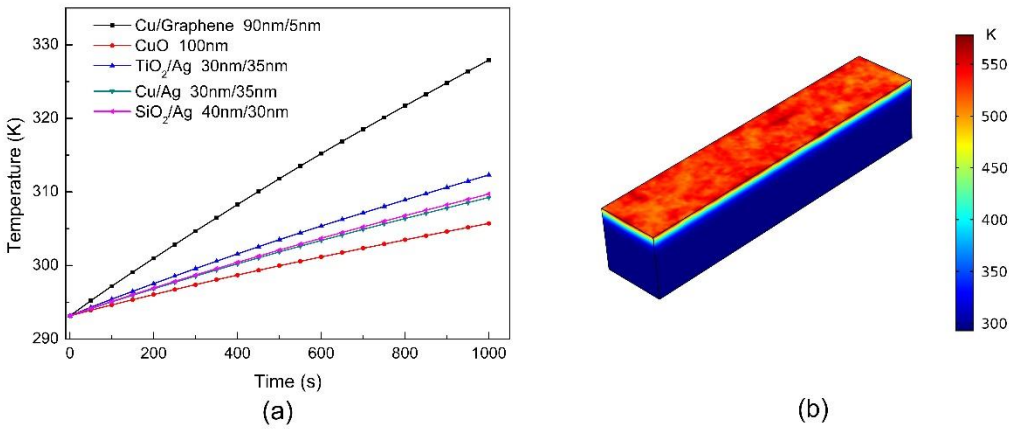

Figure 13. (a) The temperature results of cuboid model for nanofluids corresponding different nanoparticles. (b) Temperature distribution of cuboid model for Cu/Graphene nanofluids.

The nanofluids with different nanoparticle volume fraction and different incident light intensity were further investigated, as shown in Fig. 14. The volume fraction was set to be 0.001%, 0.005%, 0.01%, respectively, and pure water as a reference. The nanofluid exhibited 314.5 1/m of the absorption coefficient at φ = 0.001%, 1707.5 1/m at φ = 0.005% and 3145 1/m at φ = 0.01%. This implied the increased volume-averaged temperature rise with the volume fraction of nanoparticle in nanofluids as shown in Fig. 14a, versus almost no temperature rise in the referenced pure water which is transparent to visible light. Fig. 14b further shows the increase of the incident light intensity obviously results in the increase of volume-averaged temperature of the studied nanofluids.

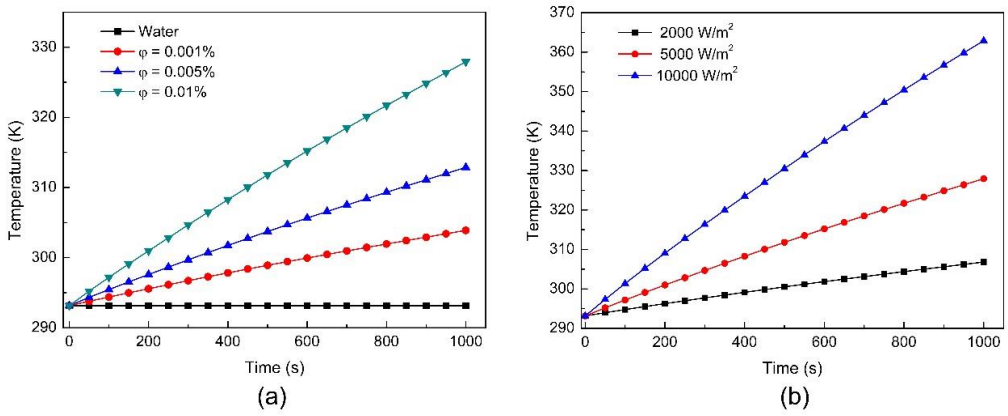

Figure 14. (a) The temperature results for Cu/Graphene nanofluids with different volume fraction of nanoparticle. (b) The temperature results for Cu/Graphene nanofluids under different incident light intensities.

Fig. 15a shows the absorption ratio varies with the depth y in different nanofluids. And H is the height of the simulation model (100 mm). It can be seen that almost all

incident light can be absorbed when the depth of nanofluids reach to 60 mm for all involved nanofluids, except for water which shows nearly no absorption of visible light. In the current case, more efficient absorption and a higher average temperature of this simulation model can be realized when the depth of nanofluid decrease to 60 mm. The allowable temperature rise was restricted by the phase change of nanofluids. In order to avoid the phase transition effect caused by excessive temperature, the heat of the system can be exported through nanofluids flow. The heat transfer for the nanofluids flow, whose flow direction was perpendicular to the incident light, was further investigated. Fig. 15b initially displays the corresponding time to reach the equilibrium steady state in the nanofluid flow. A slight increase of equilibrium volume average temperature was obtained after 50 seconds irradiation when the flow velocity to be 0.01 m/s. In contrast, the equilibrium average nanofluid temperature after 1000 seconds was found to be at 325 K when the flow velocity to be 0.0005 m/s. Fig. 16a-d further show temperature distribution of the simulating nanofluids corresponding to the variation of flow velocities.

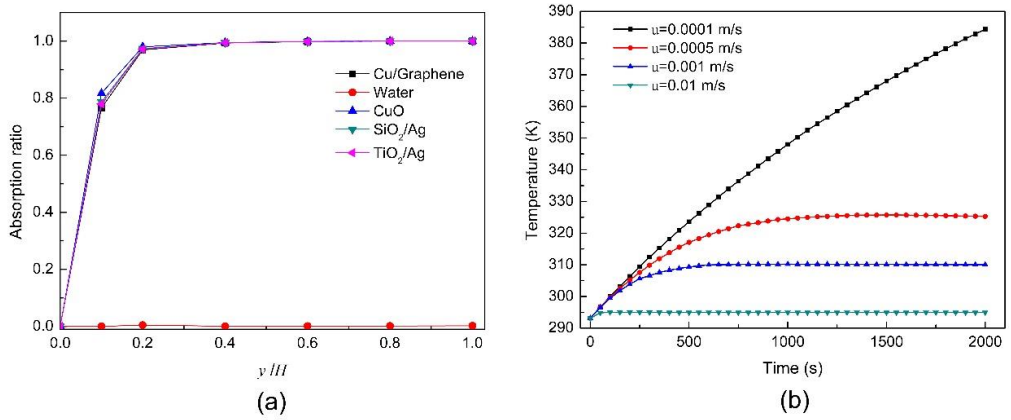

Figure 15. (a) Absorption ratio with depth of nanofluids corresponding to different nanoparticles.

(b) The temperature results for Cu/Graphene nanofluids with different flow velocities.

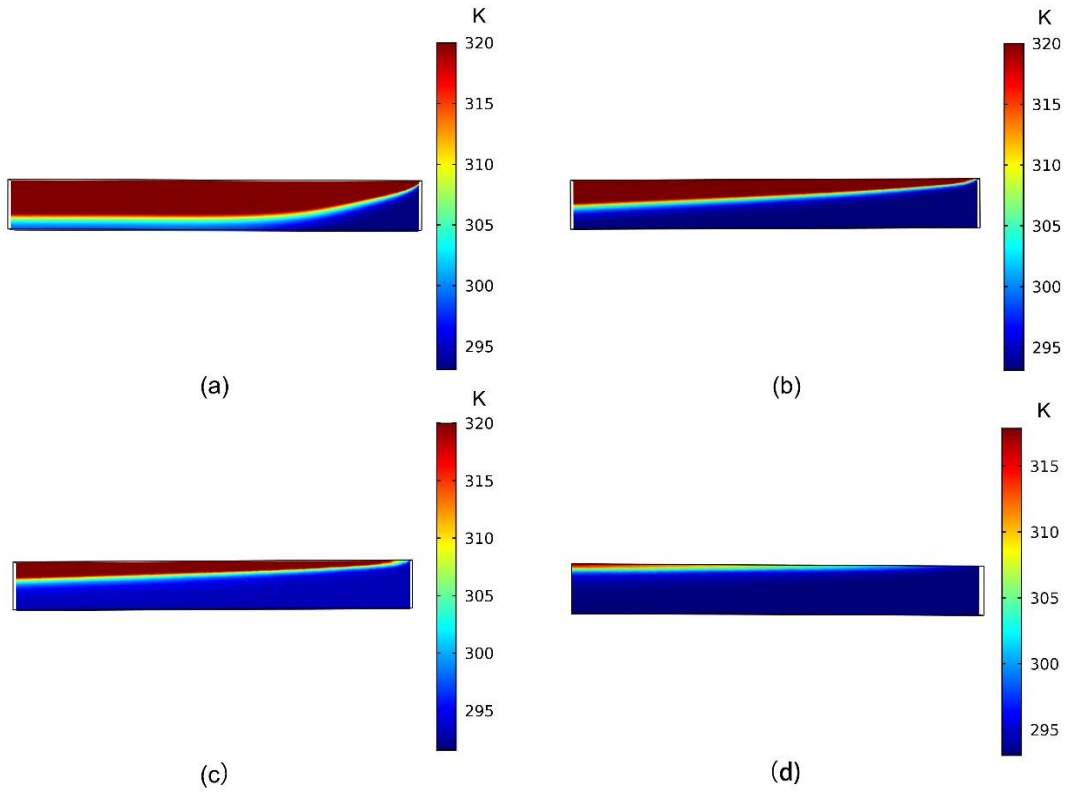

Figure 16. Profile of temperature distribution for nanofluids with different flow velocities. (a) u =0.0001 m/s. (b) u =0.0005 m/s. (c) u =0.001 m/s. (d) u =0.01 m/s.

3.1.4. Conclusion

The optical and photothermal properties of nanoparticles and nanofluids were studied using the established numerical model, and its accuracy was well verified by experimental results. Core-shell nanoparticles exhibited excellent characteristics of the LSPR frequency shift compared with those of pure noble metal nanoparticles. Among of them, a core-shell structure nanoparticle with Cu core in diameter of 90 nm coated with 5 nm thickness graphene had a better photothermal property in the desirable solar spectrum. Results revealed that not only scattering and absorption affected the

photothermal properties, also the thermodynamic properties of nanoparticles affected the photothermal conversion. Studies on a two-particle model in the simulation domain revealed the temperature of the two particle models exceeded 360 K, versus 342.44 K for the single nanoparticle case under the same irradiation condition. The temperature of uniformly-distributed eight-particle can reach over 700 K versus only about 500 K of the aggregated eight-particle, implying that highly dispersed nanoparticles were more conducive to the overall temperature rise. The Cu/Graphene core-shell nanofluids showed an excellent photothermal conversion performance. The average temperature of nanofluid corresponding Cu/Graphene core-shell nanoparticle can rise up to 328 K after the 1000 seconds irradiation at a volume fraction at 0.01%, which was much higher than that of other nanofluids. And the specific 60 mm in the depth of nanofluids can almost absorb all of the incident light. This study revealed the simulation method can provide the convenient and rapid screening of potential nanoparticles and nanofluids candidates for solar energy harvests.

3.2 Optical and photothermal properties of soot

Soot is an important anthropogenic carbonaceous aerosol that forms atmospheric smog. The atmospheric presence of smog raises great concerns about human health. Soot particles are found to be strong absorbers and scatterers of visible light, which makes up a substantial part of the solar spectrum. However, most recent studies on the optical properties of soot were restricted to the IR wavelength range [55] [56], and few studies addressed the Vis wavelength range [57] [58]. In this research, studies on the optical properties of soot particles were carried out in the full wavelength spectrum of Vis light using the FEM simulation method. First, the model of the scattering and

absorption of a single soot particle was established，and the scattering and absorption properties of different soot particles (diesel, acetylene, and propane soot) and graphite particles as the surrogate for soot were calculated in the visible wavelength range. The effectiveness of the adopted methods was verified by openly published experiments and the Mie theory. To make the simulation more similar to real soot aerosols, two major submodels were integrated, which involved their core-shell structures and their fractal agglomerate structures. The effects of different shell materials and their thickness on the optical properties of the graphite core were studied. The absorption enhancement [59] $E_{abs}=\sigma_{\text{abs-core/shell}}/\sigma_{abs-core}$ is defined to indicate the enhancement intensity of the coated particle to an equivalent uncoated particle, which is expressed as the ratio of the absorption cross section of the core/shell particle to the absorption cross section of core particle. The studied shell materials included water (H_2O), sulfuric acid (H_2SO_4), salt (NaCl) and BrC. Finally, a more realistic soot aggregation model was established based on the diffusion limited aggregation algorithm (DLA), and furthermore, the optical and photothermal properties of these aggregations were studied by multiphysics coupling based on the FEM simulation method. Thus, this study provided a new and efficient method for understanding the optical properties and warming effects of realistic soot particles.

3.2.1. Optical Properties of Different Soot Particles.

Soot particles vary according to sources and regions. This study typically involved investigations on optical properties of three kinds of soot particles and three kinds of graphite particles. First, the effectiveness of the FEM method was verified by openly

published experimental results and the Mie theory. Fig. 17a shows the extinction results of polystyrene latex spheres (PSL) with a diameter of 600 nm [60]. The dashed line represents results from the applied FEM method in this research. It was found that spectra of the PSL agreed well with each other in the same wavelength range, and the maximum extinction appeared at the wavelength of 500 nm. The missing extinction results within the wavelength range of 300 nm and 430 nm in the FEM method was due to the lack of optical constants of PSL in this range. In addition, the effectiveness of the applied FEM method was further verified by comparing the extinction results of the noble metal silver (Ag) with a diameter of 92 nm because of the abundance of experimental data (Fig. 17b) [61]. The verification supported the accuracy of the prediction of the optical properties of particles using the adopted method in this study.

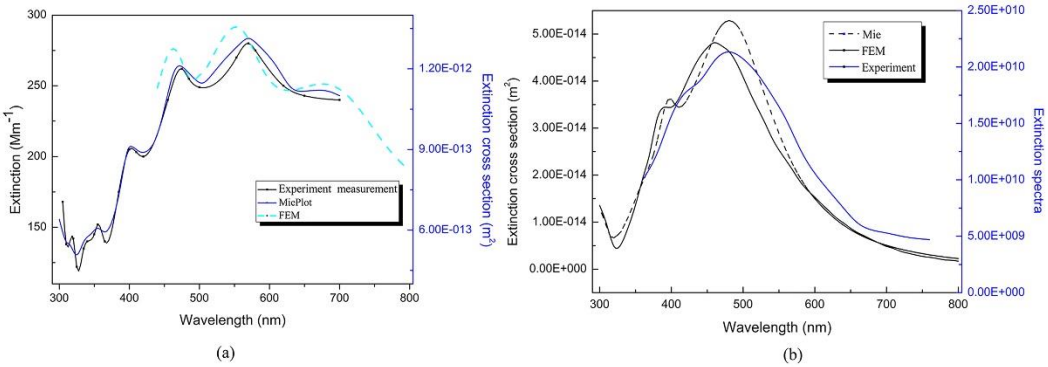

Figure 17. (a) Extinction spectra of PSL with a diameter of 600 nm via experimental, MiePlot and FEM results. (b) Extinction spectra of Ag nanoparticles with a diameter of 92 nm via experimental, MiePlot and FEM results.

Three kinds of soot particles (diesel soot [62], acetylene soot and propane soot [63]) and three carbon surrogates for soot particles (graphite 1 [64], graphite 2 and pyrolytic

carbon [65]) were used to investigate their optical properties [66]. The diameter of freshly emitted spherical soot monomer was set to 50 nm, and the studied wavelength ranged from 300 nm to 800 nm, covering the entire visible region of sunlight. Fig. 18 shows the extinction and absorption cross section of studied particles, which shows that these particles are good light absorbers because of the almost equivalent extinction and absorption cross sections. Interestingly, the extinction result of graphite 1 was close to those of acetylene soot and propane soot at the relatively longer wavelength (> 500 nm) versus that of pyrolytic carbon, which was close to that of soot particles at a short wavelength (< 400 nm). The diesel soot showed a relatively weaker extinction effect than other particles. It is notable that the aforementioned studies were based on the single particle model. Moreover, Fig. 19 shows the scattering properties of those particles that were revealed by their far-field scattering patterns. Generalized scattering patterns of the involved particles were found to exhibit the tendency of forwarding scattering in a shorter wavelength range and dipole antenna scattering for a longer wavelength range. Moreover, the graphite particles incurred stronger light scattering in a shorter wavelength range compared to that of soot particles, but scattering was comparable in the longer wavelength range.

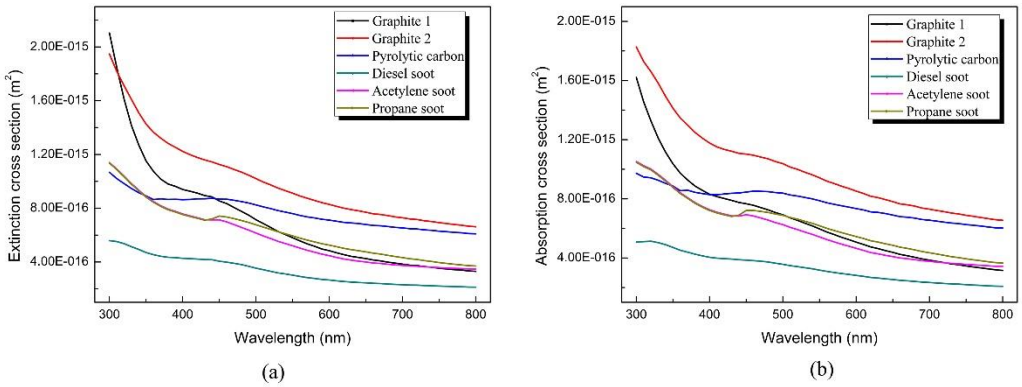

Figure 18. (a) The extinction cross section of the studied particles. (b) The absorption cross section of the studied particles.

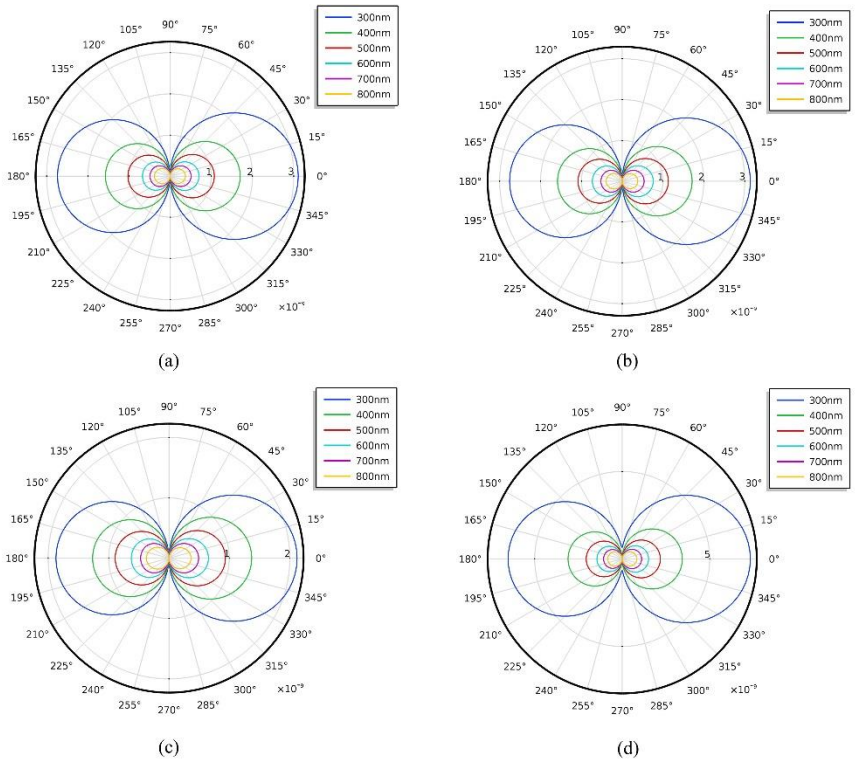

Figure 19. (a) The far-field scattering pattern of the acetylene soot. (b) The far-field scattering pattern of the propane soot. (c) The far-field scattering pattern of the diesel soot. (d) The far-field scattering pattern of the graphite 1.

3.2.2. Optical Properties of Soot Particles with Different Shell Materials.

Soot particles in the atmosphere tend to be the internal core in a core-shell mixed structure after undergoing an aging process. The treatment of these mixtures as core/shell structures have been applied and confirmed in many previous studies by investigating their microscopic images [67] [68]. However, the shell composition varies with sources and regions and usually has a non-absorbing composition. These structures have been extensively studied but there is a lack of studies about the consistency of their increasing role in absorption enhancement as a shell outside of soot particles to form a core-shell structure, especially those weak-absorbing BrC from similar emission sources [69]. This section only focused on graphite 1 as a core material, which was closer to soot particles in its optical constant and properties. Four kinds of typical atmospheric shell materials, such as H_2O, H_2SO_4 [70], NaCl [71] and BrC, and their different thicknesses, were investigated for their absorption enhancement contribution to the overall formed core-shell particles; this investigation yielded further understanding of their enhancement mechanisms.

Fig. 20 shows the absorption enhancement E_{abs} of soot particles coated with H_2O compared with bare particles. The coating shell thickness is 10 nm, 30 nm, 50 nm and 70 nm, and the ratio of water shell mass M_w and soot core mass M_g is 0.78, 4.29, 11.56 and 23.95, respectively. It is clearly seen that the water shell can effectively enhance the absorption efficiency of visible light by soot particles. The enhancement increased with the thickness of the water shell but in a decreasing tendency. The scattering electric field was also calculated in this model (Fig. 21) to further exhibit the mechanism of the interaction of the water shell with the extinction of soot particles. It can be seen that soot

particles of approximately 50 nm tended to forward scatter in a shorter wavelength range (300 nm wavelength), which can be enhanced by the water shell. Moreover, the enhancement of the forward scattering increased with the shell thickness. In addition, for longer wavelengths, the scattering of the particles was like a dipole antenna (consistent with the far-field scattering pattern in the last section). In addition to H_2O, there are other non-absorbing shell materials, including H_2SO_4 [72] and NaCl, that were also of interest because of their availability in atmospheric conditions. The results shown in Fig. 22a of the soot particle coated with H_2SO_4 showed a similar absorption enhancement effect compared to that of the soot particle coated with H_2O. However, a larger increase in E_{abs} was found when the soot particle was coated with NaCl, as shown in Fig. 22b, where E_{abs} was over 5 when the coating thickness was 50 nm.

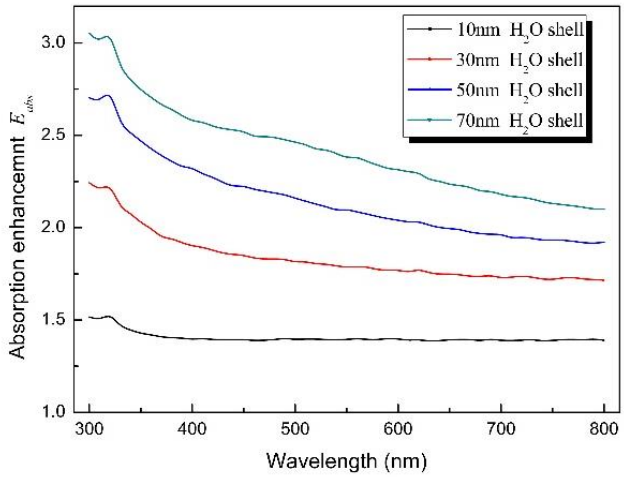

Figure 20. The absorption enhancement E_{abs} of the soot particles coated with H_2O.

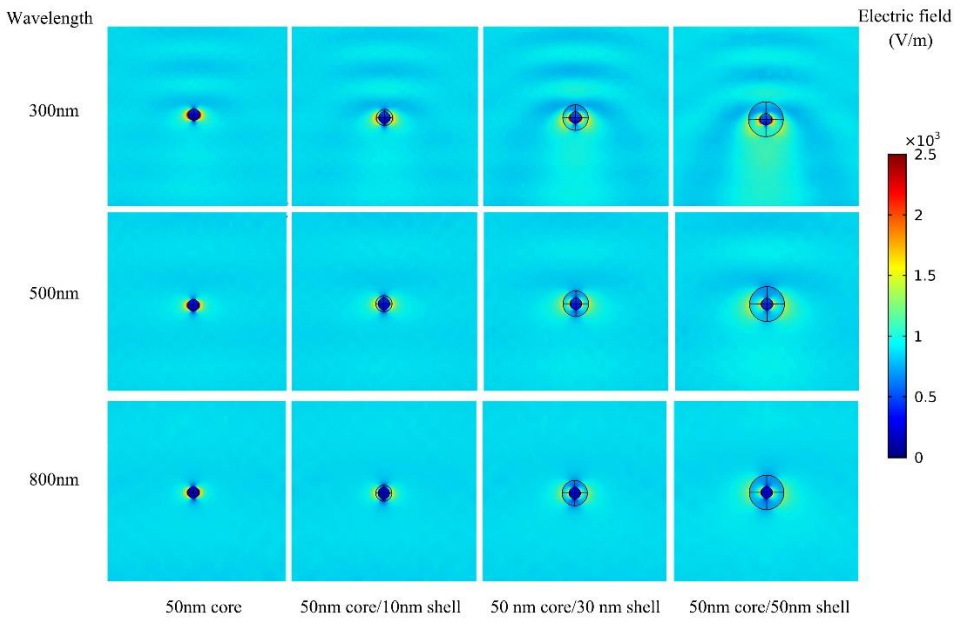

Figure 21. The scattering electric field of the soot particles coated with water shell (the incident light is from above).

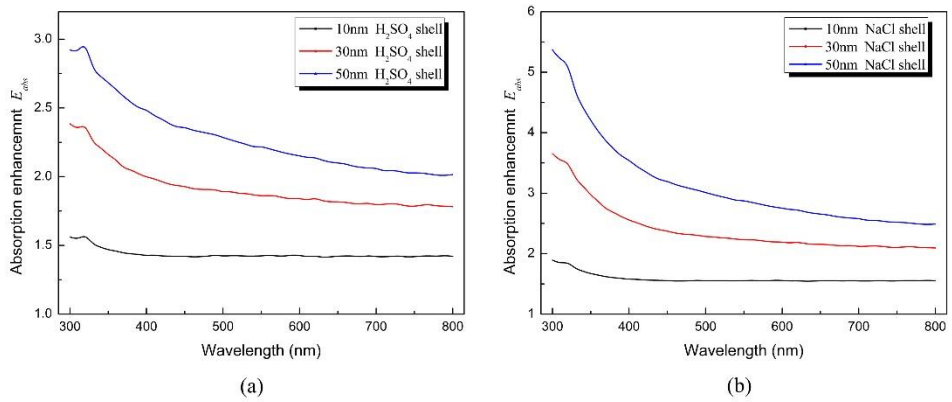

Figure 22. The absorption enhancement E_{abs} of the soot particles coated with (a) H_2SO_4 and (b) NaCl.

It is well established that the soot particles coated with the non-absorbing shell can have significant absorption of visible light. Unlike the H_2O and H_2SO_4 non-absorbing coatings, BrC was a weak-absorbing material and performed differently when coated on

soot particles. Some studies indicated that the absorption of BrC can be an important factor in aerosol radiative forcing. The refraction index of BrC can only be found at specific wavelengths in the literature [73] [74], and this literature provided a model predicting the refraction index of BrC that can be expressed as $RI = 1.7(\pm 0.2) + k_{BrC} i$. This equation helped with predicting a soot particle coated with weak absorbing BrC using the established simulation model. Fig. 23 shows the absorption enhancement of the soot particle coated with BrC, and it can be seen that BrC shells have a larger E_{abs} compared to that of the soot particle with the H_2O and H_2SO_4 shells. It was expected to find that there was a great difference of E_{abs} for soot particles with different shells, revealing that E_{abs} of soot with BrC shells was greater than those of soot with non-absorbing shells. Most significantly, E_{abs} was very different in shorter and longer wavelength ranges in the soot with greater BrC shell thickness, indicating stronger wavelength dependence of BrC shells.

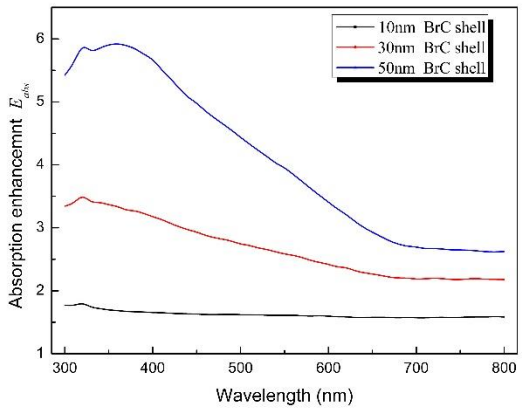

Figure 23. The absorption enhancement E_{abs} of the soot particles coated with BrC.

3.2.3. Optical Properties and Warming Effect of Soot Aggregation.

In reality, the freshly emitted soot particles tend to form aggregates due to particle collisions and water interactions, which induce the rapid aging of soot particles in a mixed state. Usually, these aggregated soot particles tend to form a compact spherical shape coated with shell materials after restructuring to reach a new stable state. In this study, DLA was applied to establish typical and relatively simple twelve-particle aggregates (50 nm diameter for each particle) for the different aging processes. The fractal dimension D_f was set to be 1.3, 2.0, and 2.8 for the three soot aggregates, such as the freshly emitted soot aggregates, the partly coated soot aggregates and the embedded soot aggregates, respectively [75] [76]. Freshly emitted soot aggregates existed as an elongated structure, while the partly coated soot aggregates was more compact and were partially surrounded by water. Embedded soot aggregates had a relatively stable structure and showed a spherical shape coated with a water shell. Fig. 24 shows the calculated absorption, scattering and extinction cross sections that revealed their optical properties. It can be seen that the freshly emitted soot aggregates and the partly coated soot aggregates had similar extinction effects. The freshly emitted aggregates tended to absorb more light, rather than scattering more light, due to their large irradiated area and small interactions between particles, while the embedded soot aggregates possessed a much stronger light extinction and the extinction cross section was close to 10000 nm^2 at the 300 nm wavelength. It can also be seen that these three soot aggregates exhibited stronger light extinction at shorter wavelengths, and there is only a small difference in the optical properties at the longer wavelengths.

To investigate the warming effect of soot particles, a model combining optics and heat

transfer was established in order to understand the photothermal behaviors of the studied particle systems. Considering the stronger extinction characteristic of soot particles at shorter wavelengths, while the solar radiation is mostly found in visible light, a focus on the incident light at 450 nm wavelength was chosen. The ambient temperature was set to be 293.15 K. Fig. 25a shows the temperature distribution around the freshly emitted soot aggregates, revealing that there was only a slight increase in temperature of the freshly emitted soot aggregates as they reached the steady state. It was also notable that the temperature varied with the polar angle θ and azimuthal angle β of the incident light due to the slender structure of freshly emitted soot aggregate (Fig. 25b). Fig. 26 shows the temperature distribution of both the partly coated soot aggregates and the embedded soot aggregates. It can be found that the temperature increase of the partly coated soot aggregates was less than that of the freshly emitted soot aggregates, which was likely attributable to the relatively compact shape of the partly coated soot aggregates and the interaction between the soot monomers. The results also revealed a maximum temperature rise, close to 0.35 K, in the case of the embedded soot aggregates due to their stronger absorption properties. Similarly, the water shell in aggregate cases can also efficiently enhance the absorption of the core structure of the soot aggregates. Overall, the optical properties and warming effects of the soot particles were related to a variety of factors, including size, shape, chemical composition and mixture state. There were still other important factors that affect the behaviors of soot, such as particle concentrations and size distributions, which encourage further research in the field.

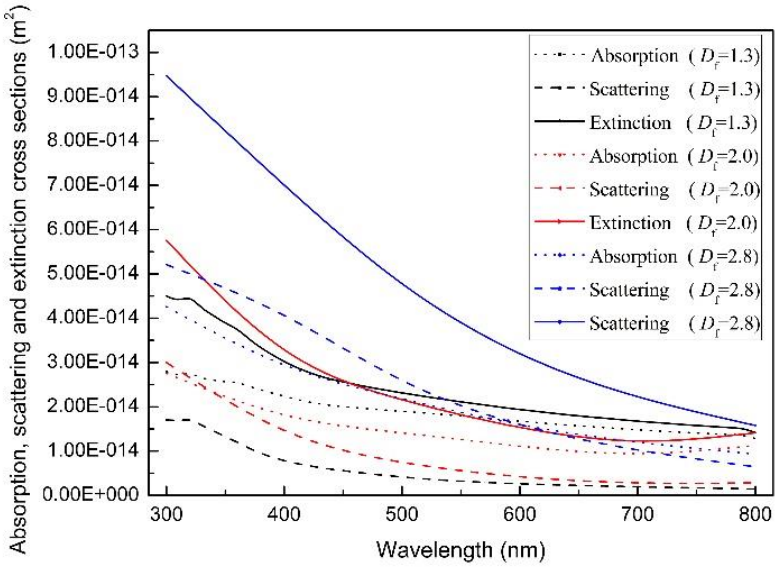

Figure 24. Absorption (dotted line), scattering (dashed line) and extinction (solid line) cross section of the soot aggregates with different shapes.

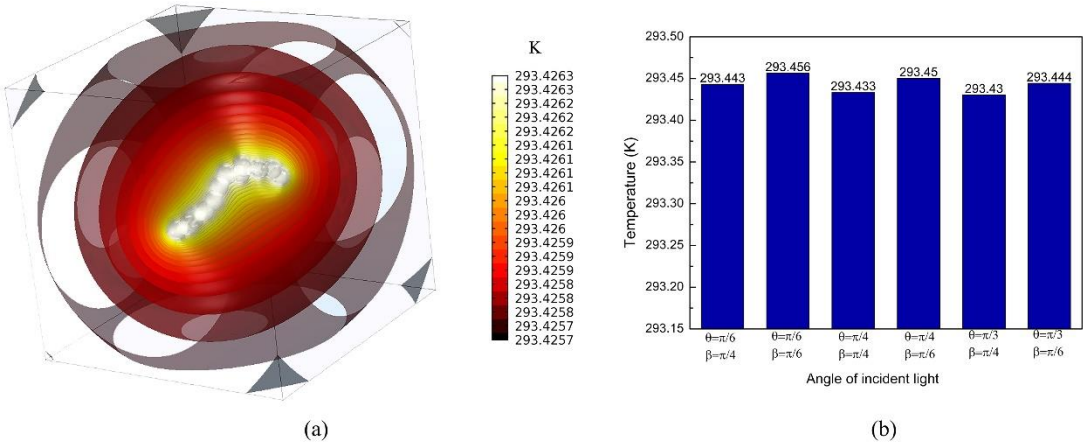

(a) (b)

Figure 25. (a) Isosurface map of the temperature distribution of freshly emitted soot aggregates. (b) Maximum temperature of the freshly emitted soot aggregates at different polar angles θ and azimuthal angles β of incident light.

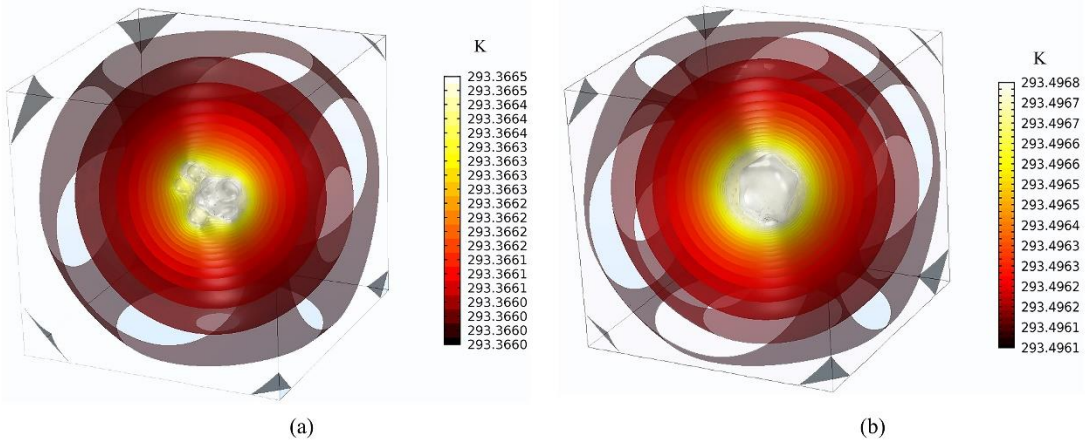

Figure 26. (a) Isosurface map of the temperature distribution of the partly coated soot aggregates. (b) Isosurface map of the temperature distribution of the embedded soot aggregates.

3.2.4. Conclusion

A numerical simulation method coupling optics and heat transfer was established to investigate the optical properties and warming effect of soot. The results are as follows,

The extinction of graphite was close to that of acetylene soot and propane soot at the relatively longer wavelength (> 500 nm), versus that of pyrolytic carbon which was close to that of soot particles at short wavelength (< 400 nm). While, the diesel soot showed a relatively weaker extinction effect than those of other particles. All of these particles tended to scatter light forward at short wavelength and showed a dipole antenna scattering at longer wavelength,

To make the simulating more realistic on real soot aerosols, two major sub-models have been integrated, which involved their core-shell structures and their fractal agglomerate structures. Four kinds of shell materials, including non-absorbing (H_2O, H_2SO_4, NaCl) and weak-absorbing (BrC) in their different shell thickness, were studied on their effects on the absorption enhancement compared to bare soot particles. All of

these shell materials can enhance the scattering forward effect at short wavelength. NaCl shell showed the strongest absorption enhancement among those non-absorbing shell materials. The absorption enhancement increased with shell thickness. However, weak-absorbing shell material BrC exhibited even better absorption enhancement (E_{abs} was close to 6 at 360 nm).

At last, three fractal soot aggregates from different aging process, such as the freshly emitted soot aggregates ($D_f = 1.3$), the partly-coated soot aggregate ($D_f = 2.0$) and the embedded soot aggregate ($D_f = 2.8$) were also investigated, and found that the embedded soot aggregate had the maximum absorption of incident light which resulted in an atmospheric temperature rising by 0.35K.

4 SUMMARY AND PROSPECT

This research provided a numerical simulation model based on FEM to study the optical properties of nanoparticles and their suspensions. The optical properties of nanoparticles consist of scattering, absorption and extinction, and in the case of nanoparticle suspension, the transmission is also included. Numerical simulation is an important auxiliary research method besides experiment. The FEM method adopted in this research is a new simulation method, which is not limited by particle shape compared with Mie theory when studying the optical properties of nanoparticles. In addition, it can couple multiple physical fields, for example, it can be coupled with the heat transfer when studying the absorption of nanoparticles to investigate the photothermal conversion of nanoparticles. Moreover, this method can also be used to conduct model transformation when studying nanoparticle suspensions.

There were two applications in this research according to the established model, one was to study the nanofluids for solar energy harvest, and the other was study the optical properties and warming effect of soot. When studying the nanofluids for solar energy harvest, this model could provide a convenient and rapid screening of potential nanoparticles and nanofluids candidates for solar energy harvests. It turned out that a core-shell structure nanoparticle with Cu core in diameter of 90 nm coated with 5 nm thickness graphene had a better photothermal property in the desirable solar spectrum. Moreover, its corresponding nanoparticle suspension, known as nanofluids, had also been studied in this research. The average temperature of nanofluid corresponding Cu/Graphene core-shell nanoparticle experienced the largest increase compared with other studied nanofluids under the same conditions. Besides, this model was also used to study the optical properties and warming effect of soot. Different soot particles were get studied in the full wavelength spectrum of Vis light. Their particle size, as well as the material, would affect their scattering and absorption of light. What's more, to make the simulation more similar to real soot aerosols, two major submodels were integrated, which involved their core-shell structures and their fractal agglomerate structures. Several shell materials and agglomeration forms were also studied due to the strong applicability of the model.

Meanwhile, the applications studied in this research were only part of the application of this model. For example, the model could also be used in medical research to study the photothermal therapy of cancer, which was also a research hotspot. In addition, the optical properties of nanoparticles can be studied comprehensively based on this model. These optical properties of nanoparticles are important for their

characterization. Therefore, studying the interaction between matter particles and electromagnetic waves based on the built model can help to choose different characterization methods and optimize the design of spectroscopy techniques. In general, this research shows a wide range of application background, which is of great significance.

5 LITERATURE CITED

[1]. Hewakuruppu, Y. L., Dombrovsky, L. A., Chen, C., Timchenko, V., Jiang, X., & Baek, S., et al. (2013). Plasmonic "pump-probe" method to study semi-transparent nanofluids. *Applied Optics, 52*(24), 6041-6050.

[2]. Taylor, R., Coulombe, S., Otanicar, T., Phelan, P., Gunawan, A., & Lv, W., et al. (2013). Small particles, big impacts: a review of the diverse applications of nanofluids. Journal of Applied Physics, 113(1), 011301.

[3]. Piella, J., Neus G. Bastús, & Puntes, V. (2016). Size-controlled synthesis of sub-10-nanometer citrate-stabilizedgold nanoparticles and related optical properties. Chemistry of Materials, 28(4), 1066-1075.

[4]. Naqvi,, Naqvi, , Samim, M. , Abdin, M. Z. , Ahmad, F. J. , & Prashant, C. K. , et al. (2010). Concentration-dependent toxicity of iron oxide nanoparticles mediated by increased oxidative stress. *International Journal of Nanomedicine, 2010*, 983.

[5]. Hassell V, M., Readman, J. W., Ranville, J. F., & Tiede, K. (2008). Nanoparticle analysis and characterization methodologies in environmental risk assessment of engineered nanoparticles. *Ecotoxicology*, 17(5), 344-361.

[6]. Tomaszewska, E., Soliwoda, K., Kadziola, K., Tkacz-Szczesna, B., Celichowski, G., & Cichomski, M., et al. (2013). Detection limits of dls and uv-vis spectroscopy in characterization of polydisperse nanoparticles colloids. *Journal of Nanomaterials,2013*, 1-10.

[7]. Cho, T. J., & Hackley, V. A. (2010). Fractionation and characterization of gold nanoparticles in aqueous solution: asymmetric-flow field flow fractionation with mals, dls, and uv–vis detection. *Analytical & Bioanalytical Chemistry, 398*(5), 2003-2018.

[8]. Kato, H., Ouchi, N., & Nakamura, A. . (2017). Simultaneous measurement of size and density of spherical particles using two-dimensional particle tracking analysis method. *Powder Technology, 315*, 68-72.

[9]. Hole, P., Sillence, K., & Claire Hannell…. (2013). Interlaboratory comparison of size measurements on nanoparticles using nanoparticle tracking analysis (nta). *Journal of Nanoparticle Research, 15*(12), 2101 (12 pp.)---2101 (12 pp.).

[10]. Filipe, V., Hawe, A., & Jiskoot, W. (2010). Critical evaluation of Nanoparticle Tracking Analysis (NTA) by NanoSight for the measurement of nanoparticles and protein aggregates. *Pharmaceutical research, 27*(5), 796-810.

[11]. Brar, S. K., & Verma, M. (2011). Measurement of nanoparticles by light-scattering techniques. *TrAC Trends in Analytical Chemistry*, *30*(1), 4-17.
[12]. Kato, H., Nakamura, A., Takahashi, K., & Kinugasa, S. (2012). Accurate size and size-distribution determination of polystyrene latex nanoparticles in aqueous medium using dynamic light scattering and asymmetrical flow field flow fractionation with multi-angle light scattering. *Nanomaterials*, *2*(1), 15-30.
[13]. Ye, M., Wang, S., & Xu, Y. (1999). An inverse technique devised from modification of annealing-evolution algorithm for particle sizing by light scattering. *Powder technology*, *104*(1), 80-83.
[14]. Clement, S., Gardner, B., Razali, W. A. W., Coleman, V. A., Jämting, Å. K., Catchpoole, H. J., ... & Zvyagin, A. (2017). Quantification of nanoparticle concentration in colloidal suspensions by a non-destructive optical method. *Nanotechnology*, *28*(47), 475702.
[15]. Finsy, R., Deriemaeker, L., Geladé, E., & Joosten, J. (1992). Inversion of static light scattering measurements for particle size distributions. *Journal of colloid and interface science*, *153*(2), 337-354.
[16]. Yang, H., Yang, H. M., Kong, P., Zhu, Y. M., Dai, S. G., & Zheng, G. (2013). Concentration measurement of particles by number fluctuation in dynamic light backscattering. *Powder technology*, *246*, 499-503.
[17]. Tontrup, C., & Gruy, F. (2000). Light backscattering by fine non-absorbing suspended particles. *Powder technology*, *107*(1-2), 1-12.
[18]. Hua, Y., Chandra, K., Dam, D. H. M., Wiederrecht, G. P., & Odom, T. W. (2015). Shape-dependent nonlinear optical properties of anisotropic gold nanoparticles. *The journal of physical chemistry letters*, *6*(24), 4904-4908.
[19]. Sun, X., Tang, H., & Dai, J. (2009). Inversion of particle size distribution from spectral extinction data using the modified beta function. *Powder Technology*, *190*(3), 292-296.
[20]. Horvath, I. T., Colinet, P., & Vetrano, M. R. (2016). Assessment of the light extinction spectroscopy technique for submicron particle characterization. *Powder technology*, *291*, 375-382.
[21]. Khlebtsov, N. G. (2008). Determination of size and concentration of gold nanoparticles from extinction spectra. *Analytical chemistry*, *80*(17), 6620-6625.
[22]. Amendola, V., & Meneghetti, M. (2009). Size evaluation of gold nanoparticles by UV− vis spectroscopy. *The Journal of Physical Chemistry C*, *113*(11), 4277-4285.
[23]. Evanoff, D. D., & Chumanov, G. (2004). Size-controlled synthesis of nanoparticles. 2. Measurement of extinction, scattering, and absorption cross sections. *The Journal of Physical Chemistry B*, *108*(37), 13957-13962.
[24]. Chen, M., He, Y., Liu, X., Zhu, J., & Liu, R. (2017). Synthesis and optical properties of size-controlled gold nanoparticles. *Powder technology*, *311*, 25-33.
[25]. Xu, N., Bai, B., Tan, Q., & Jin, G. (2013). Fast statistical measurement of aspect ratio distribution of gold nanorod ensembles by optical extinction spectroscopy. *Optics express*, *21*(3), 2987-3000.
[26]. Potenza, M. A. C., Krpetić, Ž., Sanvito, T., Cai, Q., Monopoli, M., de Araújo, J. M., ... & Dawson, K. A. (2017). Detecting the shape of anisotropic gold

nanoparticles in dispersion with single particle extinction and scattering. *Nanoscale*, *9*(8), 2778-2784.

[27]. Kelesidis, G. A., Kholghy, M. R., Zuercher, J., Robertz, J., Allemann, M., Duric, A., & Pratsinis, S. E. (2019). Light scattering from nanoparticle agglomerates. *Powder Technology*.

[28]. Mie, G. (1976). Contributions to the optics of turbid media, particularly of colloidal metal solutions. *Contributions to the optics of turbid media, particularly of colloidal metal solutions Transl. into ENGLISH from Ann. Phys., v. 25, no. 3, 1908 p 377-445*.

[29]. Retsch, M., Schmelzeisen, M., Butt, H. J., & Thomas, E. L. (2011). Visible Mie scattering in nonabsorbing hollow sphere powders. *Nano letters*, *11*(3), 1389-1394.

[30]. Sarkar, D., & Halas, N. J. (1997). General vector basis function solution of Maxwell's equations. *Physical Review E*, *56*(1), 1102.

[31]. Draine, B. T., & Flatau, P. J. (1994). Discrete-dipole approximation for scattering calculations. *JOSA A*, *11*(4), 1491-1499.

[32]. De Abajo, F. G., & Howie, A. (2002). Retarded field calculation of electron energy loss in inhomogeneous dielectrics. *Physical Review B*, *65*(11), 115418.

[33]. Theobald, D., Egel, A., Gomard, G., & Lemmer, U. (2018, May). Simulation of light scattering in clusters of nonspherical nanoparticles: an adapted T-matrix approach. In *Nanophotonics VII* (Vol. 10672, p. 1067229). International Society for Optics and Photonics.

[34]. Yu, P., Zhang, F., Li, Z., Zhong, Z., Govorov, A., Fu, L. & Wang, Z. (2018). Giant optical pathlength enhancement in plasmonic thin film solar cells using core-shell nanoparticles. *Journal of Physics D: Applied Physics*, *51*(29), 295106.

[35]. Hergert, W., & Geilhufe, R. M. (2018). *Solution of Maxwell's Equations*. *Group Theory in Solid State Physics and Photonics*.

[36]. Phan, A. D., Le, N. B., Lien, N. T., & Wakabayashi, K. (2018). Multilayered plasmonic nanostructures for solar energy harvesting. *The Journal of Physical Chemistry C*, *122*(34), 19801-19806.

[37]. Johnson, P. B., & Christy, R. W. (1972). Optical constants of the noble metals. *Physical review B*, *6*(12), 4370.

[38]. Bohren, C. F., & Huffman, D. R. (2008). *Absorption and scattering of light by small particles*. John Wiley & Sons.

[39]. Scholl, J. A., Koh, A. L., & Dionne, J. A. (2012). Quantum plasmon resonances of individual metallic nanoparticles. *Nature*, *483*(7390), 421.

[40]. Hagemann, H. J., Gudat, W., & Kunz, C. (1975). Optical constants from the far infrared to the x-ray region: Mg, Al, Cu, Ag, Au, Bi, C, and Al 2 O 3. *JOSA*, *65*(6), 742-744.

[41]. Baffou, G., Quidant, R., & García de Abajo, F. J. (2010). Nanoscale control of optical heating in complex plasmonic systems. *ACS nano*, *4*(2), 709-716.

[42]. Gorji, T. B., & Ranjbar, A. A. (2016). A numerical and experimental investigation on the performance of a low-flux direct absorption solar collector (DASC) using graphite, magnetite and silver nanofluids. *Solar Energy*, *135*, 493-505.

[43]. Wu, Y., Cheng, T., Liu, D., Allan, J. D., Zheng, L., & Chen, H. (2018). Light Absorption Enhancement of Black Carbon Aerosol Constrained by Particle Morphology. *Environmental science & technology*, *52*(12), 6912-6919.

[44]. Tyagi, H., Phelan, P., & Prasher, R. (2009). Predicted efficiency of a low-temperature nanofluid-based direct absorption solar collector. *Journal of solar energy engineering*, *131*(4), 041004.

[45]. Dang, T. M. D., Le, T. T. T., Fribourg-Blanc, E., & Dang, M. C. (2011). Synthesis and optical properties of copper nanoparticles prepared by a chemical reduction method. *Advances in Natural Sciences: Nanoscience and Nanotechnology*, *2*(1), 015009.

[46]. Jin, H., Lin, G., Bai, L., Amjad, M., Bandarra Filho, E. P., & Wen, D. (2016). Photothermal conversion efficiency of nanofluids: an experimental and numerical study. *Solar Energy*, *139*, 278-289.

[47]. Phuoc, T. X., Soong, Y., & Chyu, M. K. (2007). Synthesis of Ag-deionized water nanofluids using multi-beam laser ablation in liquids. *Optics and Lasers in Engineering*, *45*(12), 1099-1106.

[48]. Weber, J. W., Calado, V. E., & Van De Sanden, M. C. M. (2010). Optical constants of graphene measured by spectroscopic ellipsometry. *Applied Physics Letters*, *97*(9), 091904.

[49]. Woźniak, M. Diffusion Limited Aggregation (DLA) algorithm of DLA/TEM software ver. 1.13. 02.

[50]. Witten Jr, T. A., & Sander, L. M. (1981). Diffusion-limited aggregation, a kinetic critical phenomenon. *Physical review letters*, *47*(19), 1400.

[51]. He, Q., Wang, S., Zeng, S., & Zheng, Z. (2013). Experimental investigation on photothermal properties of nanofluids for direct absorption solar thermal energy systems. *Energy Conversion and Management*, *73*, 150-157.

[52]. Zeiny, A., Jin, H., Bai, L., Lin, G., & Wen, D. (2018). A comparative study of direct absorption nanofluids for solar thermal applications. *Solar Energy*, *161*, 74-82.

[53]. Xuan, Y., Duan, H., & Li, Q. (2014). Enhancement of solar energy absorption using a plasmonic nanofluid based on TiO 2/Ag composite nanoparticles. *Rsc Advances*, *4*(31), 16206-16213.

[54]. Yu, X., & Xuan, Y. (2018). Investigation on thermo-optical properties of CuO/Ag plasmonic nanofluids. *Solar Energy*, *160*, 200-207.

[55]. Sokolik, I. N., Toon, O. B., & Bergstrom, R. W. (1998). Modeling the radiative characteristics of airborne mineral aerosols at infrared wavelengths. *Journal of Geophysical Research: Atmospheres*, *103*(D8), 8813-8826.

[56]. Widmann, J. F., Yang, J. C., Smith, T. J., Manzello, S. L., & Mulholland, G. W. (2003). Measurement of the optical extinction coefficients of post-flame soot in the infrared. *Combustion and Flame*, *134*(1-2), 119-129.

[57]. Smith, A. J. A., Peters, D. M., McPheat, R., Lukanihins, S., & Grainger, R. G. (2015). Measuring black carbon spectral extinction in the visible and infrared. *Journal of Geophysical Research: Atmospheres*, *120*(18), 9670-9683.

[58]. Forestieri, S. D., Helgestad, T. M., Lambe, A. T., Renbaum-Wolff, L., Lack, D. A., Massoli, P., ... & Sedlacek III, A. J. (2018). Measurement and modeling of the

multiwavelength optical properties of uncoated flame-generated soot. *Atmospheric Chemistry and Physics*, *18*(16), 12141-12159.

[59]. Lack, D. A., & Cappa, C. D. (2010). Impact of brown and clear carbon on light absorption enhancement, single scatter albedo and absorption wavelength dependence of black carbon. *Atmospheric Chemistry and Physics*, *10*(9), 4207-4220.

[60]. Jordan, C. E., Anderson, B. E., Beyersdorf, A. J., Corr, C. A., Dibb, J. E., Greenslade, M. E., ... & Thornhill, K. L. (2015). Spectral aerosol extinction (SpEx): a new instrument for in situ ambient aerosol extinction measurements across the UV/visible wavelength range. *Atmospheric Measurement Techniques*, *8*(11), 4755-4771.

[61]. Evanoff, D. D., & Chumanov, G. (2004). Size-controlled synthesis of nanoparticles. 2. Measurement of extinction, scattering, and absorption cross sections. *The Journal of Physical Chemistry B*, *108*(37), 13957-13962.

[62]. Querry, M. (1987). *Optical constants of minerals and other materials from the millimeter to the ultraviolet* (No. CRDEC-CR-88009). Chemical Research Development And Engineering Center Aberdeen Proving Groundmd.

[63]. Dalzell, W. H., & Sarofim, A. F. (1969). Optical constants of soot and their application to heat-flux calculations. *Journal of Heat Transfer*, *91*(1), 100-104.

[64]. Taft, E. A., & Philipp, H. R. (1965). Optical properties of graphite. *Physical Review*, *138*(1A), A197.

[65]. Querry, M. (1987). *Optical constants of minerals and other materials from the millimeter to the ultraviolet* (No. CRDEC-CR-88009). Chemical Research Development And Engineering Center Aberdeen Proving Groundmd.

[66]. Shiraiwa, M., Kondo, Y., Iwamoto, T., & Kita, K. (2010). Amplification of light absorption of black carbon by organic coating. *Aerosol Science and Technology*, *44*(1), 46-54.

[67]. Chen, C., Enekwizu, O. Y., Fan, X., Dobrzanski, C. D., Ivanova, E. V., Ma, Y., ... & Khalizov, A. F. (2018). Single Parameter for Predicting the Morphology of Atmospheric Black Carbon. *Environmental science & technology*, *52*(24), 14169-14179.

[68]. Liati, A., Brem, B. T., Durdina, L., Vögtli, M., Arroyo Rojas Dasilva, Y., Dimopoulos Eggenschwiler, P., & Wang, J. (2014). Electron microscopic study of soot particulate matter emissions from aircraft turbine engines. *Environmental science & technology*, *48*(18), 10975-10983.

[69]. You, R., Radney, J. G., Zachariah, M. R., & Zangmeister, C. D. (2016). Measured wavelength-dependent absorption enhancement of internally mixed black carbon with absorbing and nonabsorbing materials. *Environmental science & technology*, *50*(15), 7982-7990.

[70]. Redemann, J., Russell, P. B., & Hamill, P. (2001). Dependence of aerosol light absorption and single‐scattering albedo on ambient relative humidity for sulfate aerosols with black carbon cores. *Journal of Geophysical Research: Atmospheres*, *106*(D21), 27485-27495.

[71]. Li, H. H. (1976). Refractive index of alkali halides and its wavelength and temperature derivatives. *Journal of physical and chemical reference data*, *5*(2), 329-528.

[72]. Palmer, K. F., & Williams, D. (1975). Optical constants of sulfuric acid; application to the clouds of Venus. *Applied Optics*, *14*(1), 208-219.

[73]. Saleh, R., Robinson, E. S., Tkacik, D. S., Ahern, A. T., Liu, S., Aiken, A. C. & Donahue, N. M. (2014). Brownness of organics in aerosols from biomass burning linked to their black carbon content. *Nature geoscience*, *7*(9), 647.

[74]. Saleh, R., Marks, M., Heo, J., Adams, P. J., Donahue, N. M., & Robinson, A. L. (2015). Contribution of brown carbon and lensing to the direct radiative effect of carbonaceous aerosols from biomass and biofuel burning emissions. *Journal of Geophysical Research: Atmospheres*, *120*(19).

[75]. Schnitzler, E. G., Dutt, A., Charbonneau, A. M., Olfert, J. S., & Jäger, W. (2014). Soot aggregate restructuring due to coatings of secondary organic aerosol derived from aromatic precursors. *Environmental science & technology*, *48*(24), 14309-14316.

[76]. Khalizov, A. F., Lin, Y., Qiu, C., Guo, S., Collins, D., & Zhang, R. (2013). Role of OH-initiated oxidation of isoprene in aging of combustion soot. *Environmental science & technology*, *47*(5), 2254-2263.